Measurement of the resonant and CP components in B¯[superscript 0]-->J/#π+π− decays

PHYSICAL REVIEW D **90,** 012003 (2014)

Measurement of the resonant and *CP* components in $\bar{B}^0 \to J/\psi\pi^+\pi^-$ decays

R. Aaij *et al.*[*]
(LHCb Collaboration)

(Received 22 April 2014; published 10 July 2014)

The resonant structure of the reaction $\bar{B}^0 \to J/\psi\pi^+\pi^-$ is studied using data from 3 fb^{-1} of integrated luminosity collected by the LHCb experiment, one third at 7 TeV center-of-mass energy and the remainder at 8 TeV. The invariant mass of the $\pi^+\pi^-$ pair and three decay angular distributions are used to determine the fractions of the resonant and nonresonant components. Six interfering $\pi^+\pi^-$ states, $\rho(770)$, $f_0(500)$, $f_2(1270)$, $\rho(1450)$, $\omega(782)$ and $\rho(1700)$, are required to give a good description of invariant mass spectra and decay angular distributions. The positive and negative charge parity fractions of each of the resonant final states are determined. The $f_0(980)$ meson is not seen and the upper limit on its presence, compared with the observed $f_0(500)$ rate, is inconsistent with a model where these scalar mesons are formed from two quarks and two antiquarks (tetraquarks) at the eight standard deviation level. In the $q\bar{q}$ model, the absolute value of the mixing angle between the $f_0(980)$ and the $f_0(500)$ scalar mesons is limited to be less than 17° at 90% confidence level.

DOI: 10.1103/PhysRevD.90.012003 PACS numbers: 14.40.Nd, 12.39.-x, 13.25.Hw, 14.40.Be

I. INTRODUCTION

The decay mode $\bar{B}^0 \to J/\psi\pi^+\pi^-$ is of particular interest in the study of charge parity (CP) violation in the B system.[1] The decay can proceed either via a tree level process, shown in Fig. 1(a), or via the penguin mechanisms shown in Fig. 1(b). The ratio of penguin to tree amplitudes is enhanced in this decay relative to $\bar{B}^0 \to J/\psi K^0_S$ [1]. Thus, the effects of penguin topologies can be investigated by using the $J/\psi\pi^+\pi^-$ decay and comparing different measurements of the CP violating phase, β, in $J/\psi K^0_S$, and individual channels such as $\bar{B}^0 \to J/\psi\rho^0$.

The $\bar{B}^0 \to J/\psi\pi^+\pi^-$ decay is also useful for the study of the substructure of light mesons that decay into $\pi^+\pi^-$. Tests have been proposed to ascertain if the scalar $f_0(500)$ and $f_0(980)$ mesons are formed of $q\bar{q}$ or tetraquarks. In the model of Ref. [2], if these scalar states are tetraquarks, the ratio of decay widths is predicted to be 1/2. If instead these are $q\bar{q}$ states, they can be mixtures of two base states; in this scenario the width ratio can be any value and is determined principally by the mixing angle between the base states.

The $\bar{B}^0 \to J/\psi\pi^+\pi^-$ decay was first observed by the *BABAR* Collaboration [3]. It has been previously studied by LHCb using data from 1 fb^{-1} of integrated luminosity [4]. The branching fraction was measured to be $(3.97 \pm 0.22) \times 10^{-5}$. The mass and angular distributions were used to measure the resonant substructure. That analysis, however, did not use the angle between the J/ψ and $\pi^+\pi^-$ decay planes, due to limited statistics. A new theoretical approach [5] now allows us to include all the angular information and measure the fraction of CP even and CP odd states. This information is vital to any subsequent CP violation measurements.

II. DATA SAMPLE AND DETECTOR

In this paper, we measure the resonant substructure and CP content of the $\bar{B}^0 \to J/\psi\pi^+\pi^-$ decay from data corresponding to 3 fb^{-1} of integrated luminosity collected with the LHCb detector [6] using pp collisions. One third of the data was acquired at a center-of-mass energy of 7 TeV, and the remainder at 8 TeV. The detector is a single-arm forward spectrometer covering the pseudorapidity range $2 < \eta < 5$, designed for the study of particles containing b or c quarks. The detector includes a high-precision tracking system consisting of a silicon-strip vertex detector surrounding the pp interaction region, a large-area silicon-strip detector located upstream of a dipole magnet with a bending power of about 4 Tm, and three stations of silicon-strip detectors and straw drift tubes [7] placed downstream. The combined tracking system provides a momentum measurement with relative uncertainty that varies from 0.4% at 5 GeV to 0.6% at 100 GeV,[2] and an impact parameter (IP) resolution of 20 μm for tracks with large transverse momentum (p_T). Different types of charged hadrons are distinguished by information from two ring-imaging Cherenkov (RICH) detectors [8]. Photon, electron and hadron candidates are identified by

[*] Full author list given at the end of the article.

[1] In this paper, mention of a particular decay mode implies the use of the charge conjugate decay as well, unless stated otherwise.

[2] We work in units where $c = 1$.

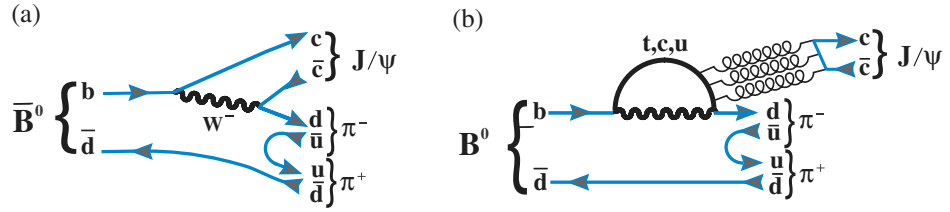

FIG. 1 (color online). (a) Tree level and (b) penguin diagram for $\bar{B}^0$ decays into $J/\psi\pi^+\pi^-$.

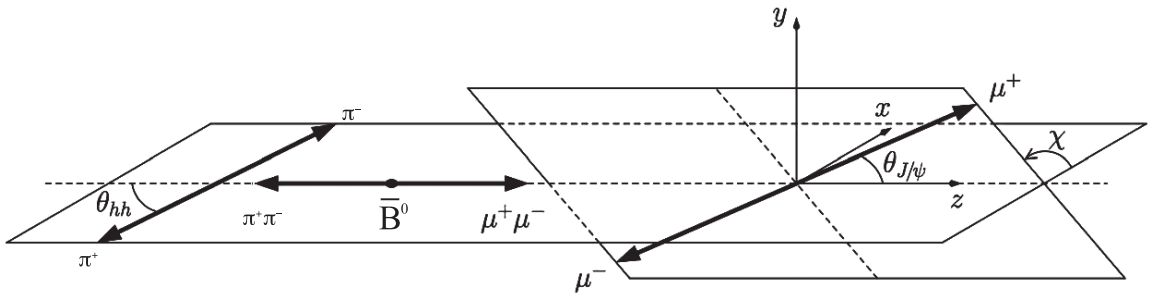

FIG. 2. Illustration of the three angles used in this analysis.

a calorimeter system consisting of scintillating-pad and preshower detectors, an electromagnetic calorimeter and a hadronic calorimeter. Muons are identified by a system composed of alternating layers of iron and multiwire proportional chambers [9].

The trigger consists of a hardware stage, based on information from the calorimeter and muon systems, followed by a software stage that applies a full event reconstruction [10]. Events selected for this analysis are triggered by a $J/\psi \to \mu^+\mu^-$ decay, where the J/ψ meson is required at the software level to be consistent with coming from the decay of a $\bar{B}^0$ meson by use either of IP requirements or detachment of the J/ψ meson decay vertex from the primary vertex (PV). In the simulation, pp collisions are generated using PYTHIA [11] with a specific LHCb configuration [12]. Decays of hadronic particles are described by EVTGEN [13], in which final state radiation is generated using PHOTOS [14]. The interaction of the generated particles with the detector and its response are implemented using the GEANT4 toolkit [15,16] as described in Ref. [17].

III. DECAY AMPLITUDE FORMALISM

A. Observables used in the analysis

The $\bar{B}^0 \to J/\psi\pi^+\pi^-$ decay with $J/\psi \to \mu^+\mu^-$ can be described by the invariant mass of the $\pi^+\pi^-$ (m_{hh}) pair, and three angles: (i) the angle between the μ^+ direction in the J/ψ rest frame with respect to the J/ψ direction in the $\bar{B}^0$ rest frame, $\theta_{J/\psi}$; (ii) the angle between the π^+ direction and the opposite direction of the $\bar{B}^0$ candidate momentum in the $\pi^+\pi^-$ rest frame, θ_{hh}; and (iii) the angle between the J/ψ and $\pi^+\pi^-$ decay planes in the $\bar{B}^0$ rest frame, χ. The angular variables are illustrated in Fig. 2.

In our previous study [4], we used the "Dalitz-plot" variables: the invariant mass squared of $J/\psi\pi^+$, $s_{12} = m^2(J/\psi\pi^+)$, and the invariant mass squared of the $\pi^+\pi^-$ pair, $s_{23} = m^2(\pi^+\pi^-)$. Due to the J/ψ spin, the event distributions in the s_{12} and s_{23} plane do not directly show the effect of the matrix-element squared. Since the probability density functions (PDFs) expressed as functions of m_{hh} and θ_{hh} are easier to normalize, we use them instead. In this paper, the notation hh is equivalent to $\pi^+\pi^-$. The Dalitz-plot variables can be translated into (m_{hh}, θ_{hh}), and vice versa. The formalism described below is for the decay sequence $\bar{B}^0 \to J/\psi R$, $R \to \pi^+\pi^-$.

B. AMPLITUDE FORMALISM

The decay rate of $\overset{(-)}{B}{}^0 \to J/\psi\pi^+\pi^-$ has been described in detail in Ref. [5]. The differential decay width can be written in terms of the decay time t and the four other variables $m_{hh}, \theta_{J/\psi}, \theta_{hh}$ and χ as [18]

$$\frac{d^5\Gamma}{dt dm_{hh} d\cos\theta_{J/\psi} d\cos\theta_{hh} d\chi} = \mathcal{N} e^{-\Gamma t}\left\{\frac{|A|^2 + |(q/p)\bar{A}|^2}{2}\cosh\frac{\Delta\Gamma t}{2} + \frac{|A|^2 - |(q/p)\bar{A}|^2}{2}\cos(\Delta m t) - \mathcal{R}e((q/p)A^*\bar{A})\,\sinh\frac{\Delta\Gamma t}{2} - \mathcal{I}m((q/p)A^*\bar{A})\,\sin(\Delta m t)\right\}, \quad (1)$$

$$\frac{d^5\bar{\Gamma}}{dt dm_{hh} d\cos\theta_{J/\psi} d\cos\theta_{hh} d\chi} = \left|\frac{p}{q}\right|^2 \mathcal{N} e^{-\Gamma t}\left\{\frac{|A|^2+|(q/p)\bar{A}|^2}{2}\cosh\frac{\Delta\Gamma t}{2} - \frac{|A|^2-|(q/p)\bar{A}|^2}{2}\cos(\Delta m t) - \mathcal{R}e((q/p)A^*\bar{A})\sinh\frac{\Delta\Gamma t}{2} + \mathcal{I}m((q/p)A^*\bar{A})\sin(\Delta m t)\right\}, \quad (2)$$

where $\mathcal{N}$ is a constant; $\overset{(-)}{A}$ is the amplitude of $\overset{(-)}{B}{}^0 \to J/\psi\pi^+\pi^-$ at the decay time $t=0$, which is itself a function of $m_{hh}, \theta_{J/\psi}, \theta_{hh}$ and χ, summed over all resonant (and possibly nonresonant) components; Δm is the mass difference between the heavy and light B^0 mass eigenstates and $\Delta\Gamma$ the width difference;[3] q and p are complex parameters that describe the relation between mass and flavor eigenstates. In this analysis we take $|p/q|$ to be equal to unity.

Forming the sum of B^0 and $\bar{B}^0$ decay widths and integrating over decay time yields the time-integrated and flavor-averaged decay width

$$S(m_{hh},\theta_{hh},\theta_{J/\psi},\chi) = |A(m_{hh},\theta_{hh},\theta_{J/\psi},\chi)|^2 + |\bar{A}(m_{hh},\theta_{hh},\theta_{J/\psi},\chi)|^2 - 2\mathcal{D}\mathcal{R}e\left(\frac{q}{p}A^*(m_{hh},\theta_{hh},\theta_{J/\psi},\chi)\bar{A}(m_{hh},\theta_{hh},\theta_{J/\psi},\chi)\right) \approx |A(m_{hh},\theta_{hh},\theta_{J/\psi},\chi)|^2 + |\bar{A}(m_{hh},\theta_{hh},\theta_{J/\psi},\chi)|^2, \quad (3)$$

where we drop the term arising from quantum interference of the amplitudes in the last line. This results from the fact that the $\mathcal{D}$ factor is negligibly small for $\bar{B}^0$ meson decays. Specifically,

$$\mathcal{D} = \frac{\int_0^\infty \alpha(t) e^{-\Gamma t}\sinh\frac{\Delta\Gamma t}{2}\mathrm{d}t}{\int_0^\infty \alpha(t) e^{-\Gamma t}\cosh\frac{\Delta\Gamma t}{2}\mathrm{d}t}, \quad (4)$$

where $\alpha(t)$ is the decay time dependent detection efficiency.[4] Since $\Delta\Gamma/\Gamma$ is of the order of 1% for $\bar{B}^0$ meson decays [19], the $\mathcal{D}$ term is about the same size.

We define $A_R(m_{hh})$ to be the mass line shape of the resonance R, which in most cases is a Breit-Wigner function. It is combined with the decay properties of the $\bar{B}^0$ and resonance to form the expression for the decay amplitude. For each resonance R,

$$\mathcal{A}_R(m_{hh}) = \sqrt{2J_R+1}\sqrt{P_R P_B}F_B^{(L_B)}\left(\frac{P_B}{m_B}\right)^{L_B} \times F_R^{(L_R)}\left(\frac{P_R}{m_{hh}}\right)^{L_R} A_R(m_{hh}). \quad (5)$$

Here P_R (P_B) is the scalar momentum of one of the two daughters of the resonance R (or the $\bar{B}^0$ meson) in the R (or $\bar{B}^0$) rest frame, J_R is the spin of R, L_B is the orbital angular momentum between the J/ψ and h^+h^- system, and L_R the orbital angular momentum in the h^+h^- decay, and thus is the same as the spin of the h^+h^- resonance. $F_B^{(L_B)}$ and $F_R^{(L_R)}$ are the centrifugal barrier factors for the $\bar{B}^0$ and the R resonance, respectively [20]. The factor $\sqrt{P_R P_B}$ results from converting the phase space of the Dalitz-plot variables m_{hh}^2 and $m_{J/\psi h^+}^2$ to that of m_{hh} and $\cos\theta_{hh}$. The function defined in Eq. (5) is based on previous amplitude analyses [20,21].

We must sum over all final states, R, so for each J/ψ helicity, denoted by λ, equal to 0, +1 and −1 we have the overall decay amplitudes

$$\overset{(-)}{\mathcal{H}}_\lambda(m_{hh},\theta_{hh}) = \sum_R \overset{(-)}{\mathbf{h}}{}_\lambda^R \mathcal{A}_R(m_{hh}) d^{J_R}_{-\lambda,0}(\theta_{hh}), \quad (6)$$

where the Wigner-d functions are defined in Ref. [19] and $\overset{(-)}{\mathbf{h}}{}_\lambda^R$ are complex helicity coefficients. We note that the λ value of the J/ψ is equal to that of the R resonance. Finally, the total decay rate of $\overset{(-)}{B}{}^0 \to J/\psi\pi^+\pi^-$ at $t=0$ is given by

$$|\overset{(-)}{A}(m_{hh},\theta_{hh},\theta_{J/\psi},\chi)|^2 = \Big|\overset{(-)}{\mathcal{H}}_0(m_{hh},\theta_{hh})|^2\sin^2\theta_{J/\psi} + \frac{1}{2}(|\overset{(-)}{\mathcal{H}}_+(m_{hh},\theta_{hh})|^2 + |\overset{(-)}{\mathcal{H}}_-(m_{hh},\theta_{hh})|^2)(1+\cos^2\theta_{J/\psi}) + \mathcal{R}e[\overset{(-)}{\mathcal{H}}_+(m_{hh},\theta_{hh})\overset{(-)*}{\mathcal{H}}_-(m_{hh},\theta_{hh})e^{2i\chi}]\sin^2\theta_{J/\psi} + \sqrt{2}\mathcal{R}e[(\overset{(-)}{\mathcal{H}}_0(m_{hh},\theta_{hh})\overset{(-)*}{\mathcal{H}}_+(m_{hh},\theta_{hh}) - \overset{(-)*}{\mathcal{H}}_0(m_{hh},\theta_{hh})\overset{(-)}{\mathcal{H}}_-(m_{hh},\theta_{hh}))e^{-i\chi}]\sin\theta_{J/\psi}\cos\theta_{J/\psi}. \quad (7)$$

[3]We use the conventions that $\Delta m = m_H - m_L$ and $\Delta\Gamma = \Gamma_L - \Gamma_H$, where L and H correspond to the light and heavy mass eigenstates, respectively.

[4]For uniform acceptance, $\mathcal{D} = \Delta\Gamma/(2\Gamma)$.

TABLE I. *CP* parity of the full final state for different spin resonances. Note that spin 0 only has the 0 transversity component.

Spin	η_0	$\eta_\parallel$	$\eta_\perp$
0	−1		
1	1	1	−1
2	−1	−1	1

In order to determine the *CP* components, it is convenient to replace the complex helicity coefficients $\overset{(-)}{\mathbf{h}}{}^R_\lambda$ by the complex transversity coefficients $\overset{(-)}{\mathbf{a}}{}^R_\tau$ using the relations

$$\begin{aligned}
\overset{(-)}{\mathbf{h}}{}^R_0 &= \overset{(-)}{\mathbf{a}}{}^R_0, \\
\overset{(-)}{\mathbf{h}}{}^R_+ &= \frac{1}{\sqrt{2}}(\overset{(-)}{\mathbf{a}}{}^R_\parallel + \overset{(-)}{\mathbf{a}}{}^R_\perp), \\
\overset{(-)}{\mathbf{h}}{}^R_- &= \frac{1}{\sqrt{2}}(\overset{(-)}{\mathbf{a}}{}^R_\parallel - \overset{(-)}{\mathbf{a}}{}^R_\perp).
\end{aligned} \tag{8}$$

Here $\overset{(-)}{\mathbf{a}}{}^R_0$ corresponds to the longitudinal polarization of the J/ψ meson, and the other two coefficients correspond to polarizations of the J/ψ meson and h^+h^- system transverse to the decay axis: $\overset{(-)}{\mathbf{a}}{}^R_\parallel$ for parallel polarization of the J/ψ and h^+h^-, and $\overset{(-)}{\mathbf{a}}{}^R_\perp$ for perpendicular polarization.

Assuming the absence of direct *CP* violation, the relation between the $\bar{B}^0$ and B^0 transversity coefficients is $\bar{\mathbf{a}}^R_\tau = \eta^R_\tau \mathbf{a}^R_\tau$, where η^R_τ is the *CP* eigenvalue of the τ transversity component for the intermediate state R, and τ denotes the $0, \parallel$ or $\perp$ components. Note that for the h^+h^- system both C and P are given by $(-1)^{L_R}$, so the *CP* of the h^+h^- system is always even. The total *CP* of the final state is $(-1)^{L_B}$, since the *CP* of the J/ψ is also even. The final state *CP* parities, for S, P and D waves, are listed in Table I.

In this analysis a fit determines the amplitude modulus a^R_τ and the phase ϕ^R_τ of the amplitude

$$\mathbf{a}^R_\tau = a^R_\tau e^{i\phi^R_\tau} \tag{9}$$

for each resonance R and each transversity component τ. For the $\tau = \perp$ amplitude, the L_B value of spin-1 (or spin-2) resonances is 1 (or 2). While the other transversity components, $\tau = 0$ or $\parallel$, have two possible L_B values of 0 and 2 (or 1 and 3) for spin-1 (or -2) resonances. We use only the smaller values for each. Studies show that our results for fractions of different interfering components are not sensitive to these L_B choices.

C. Dalitz fit fractions

A complete description of the decay is given in terms of the fitted complex amplitudes. Knowledge of the contribution of each component can be summarized by defining a fit fraction for each transversity τ, $\mathcal{F}^R_\tau$. To determine $\mathcal{F}^R_\tau$ one needs to integrate over all of the four variables: $m_{hh}, \theta_{hh}, \theta_{J/\psi}, \chi$. The interference terms between different helicity components vanish after integrating Eq. (7) over the two variables of $\cos\theta_{J/\psi}$ and χ, i.e.

$$\int |\overset{(-)}{A}(m_{hh}, \theta_{hh}, \theta_{J/\psi}, \chi)|^2 d\cos\theta_{J/\psi} d\chi = \frac{4}{3}(|\overset{(-)}{\mathcal{H}}_0(m_{hh}, \theta_{hh})|^2 + |\overset{(-)}{\mathcal{H}}_+(m_{hh}, \theta_{hh})|^2 + |\overset{(-)}{\mathcal{H}}_-(m_{hh}, \theta_{hh})|^2). \tag{10}$$

The decay rate is the sum of the contributions from the three helicity terms. To define the transversity fractions, we need to write Eq. (10) in terms of transversity amplitudes. Since $d^{J_R}_{-1,0} = -d^{J_R}_{1,0}$, the sum of the three helicity terms is equal to the sum of three transversities, given as

$$\begin{aligned}
&|\mathcal{H}_0(m_{hh}, \theta_{hh})|^2 + |\mathcal{H}_+(m_{hh}, \theta_{hh})|^2 + |\mathcal{H}_-(m_{hh}, \theta_{hh})|^2 \\
&\quad = \left|\sum\nolimits_R \mathbf{a}^R_0 \mathcal{A}_R(m_{hh}) d^{J_R}_{0,0}(\theta_{hh})\right|^2 + \left|\sum\nolimits_R \mathbf{a}^R_\parallel \mathcal{A}_R(m_{hh}) d^{J_R}_{1,0}(\theta_{hh})\right|^2 + \left|\sum\nolimits_R \mathbf{a}^R_\perp \mathcal{A}_R(m_{hh}) d^{J_R}_{1,0}(\theta_{hh})\right|^2.
\end{aligned} \tag{11}$$

Thus, we define the transversity fit fractions as

$$\mathcal{F}^R_\tau = \frac{\int |a^R_\tau e^{i\phi^R_\tau} \mathcal{A}_R(m_{hh}) d^{J_R}_{\lambda,0}(\theta_{hh})|^2 dm_{hh} d\cos\theta_{hh}}{\int (|\mathcal{H}_0(m_{hh}, \theta_{hh})|^2 + |\mathcal{H}_+(m_{hh}, \theta_{hh})|^2 + |\mathcal{H}_-(m_{hh}, \theta_{hh})|^2) dm_{hh} d\cos\theta_{hh}}, \tag{12}$$

where $\lambda = 0$ for $\tau = 0$, and $\lambda = 1$ for $\tau = \perp$ or $\parallel$.

The sum of the fit fractions is not necessarily unity due to the potential presence of interference between two resonances. Interference term fractions are given by

$$\mathcal{F}_\tau^{RR'} = 2\mathcal{R}e\left(\frac{\int a_\tau^R a_\tau^{R'} e^{i(\phi_\tau^R-\phi_\tau^{R'})}\mathcal{A}_R(m_{hh})\mathcal{A}^*_{R'}(m_{hh})d^{J_R}_{\lambda,0}(\theta_{hh})d^{J_{R'}}_{\lambda,0}(\theta_{hh})dm_{hh}d\cos\theta_{hh}}{\int(|\mathcal{H}_0(m_{hh},\theta_{hh})|^2+|\mathcal{H}_+(m_{hh},\theta_{hh})|^2+|\mathcal{H}_-(m_{hh},\theta_{hh})|^2)dm_{hh}d\cos\theta_{hh}}\right), \quad (13)$$

and

$$\sum_{R,\tau}\mathcal{F}_\tau^R + \sum_{RR',\tau}^{R>R'}\mathcal{F}_\tau^{RR'} = 1. \quad (14)$$

Interference between different spin-J states vanishes when integrated over angle, because the $d^J_{\lambda 0}$ angular functions are orthogonal.

IV. SELECTION REQUIREMENTS

In this analysis we adopt a two step selection. The first step, preselection, is followed by a multivariate selection based on a boosted decision tree (BDT) [22]. Preselection criteria are implemented to preserve a large fraction of the signal events, yet reject easily eliminated backgrounds, and are identical to those used in Ref. [4]. A $\bar{B}^0 \to J/\psi\pi^+\pi^-$ candidate is reconstructed by combining a $J/\psi \to \mu^+\mu^-$ candidate with two pions of opposite charge. To ensure good track reconstruction, each of the four particles in the $\bar{B}^0$ candidate is required to have the track fit χ^2/ndf to be less than 4, where ndf is the number of degrees of freedom of the fit. The $J/\psi \to \mu^+\mu^-$ candidate is formed by two identified muons of opposite charge having $p_{\rm T}$ greater than 500 MeV, and with a geometrical fit vertex χ^2 less than 16. Only candidates with dimuon invariant mass between -48 and $+43$ MeV from the observed J/ψ mass peak are selected, and are then constrained to the J/ψ mass [19] for subsequent use.

Each pion candidate is required to have $p_{\rm T}$ greater than 250 MeV, and the scalar sum, $p_{\rm T}(\pi^+) + p_{\rm T}(\pi^-)$, is required to be larger than 900 MeV. Both pions must have $\chi^2_{\rm IP}$ greater than 9 to reject particles produced from the PV. The $\chi^2_{\rm IP}$ is computed as the difference between the χ^2 of the PV reconstructed with and without the considered track. Both pions must also come from a common vertex with χ^2/ndf < 16, and form a vertex with the J/ψ with a χ^2/ndf less than 10 (here ndf equals five). Pion candidates are identified using the RICH and muon systems. The particle identification makes use of the logarithm of the likelihood ratio comparing two particle hypotheses (DLL). For the pion selection we require $\mathrm{DLL}(\pi - K) > -10$ and $\mathrm{DLL}(\pi - \mu) > -10$. The $\bar{B}^0$ candidate must have a flight distance of more than 1.5 mm. The angle between the combined momentum vector of the decay products and the vector formed from the positions of the PV and the decay vertex (pointing angle) is required to be less than 2.5°.

The BDT uses eight variables that are chosen to provide separation between signal and background. These are the minimum of $\mathrm{DLL}(\mu - \pi)$ of the μ^+ and μ^-, $p_{\rm T}(\pi^+) + p_{\rm T}(\pi^-)$, the minimum of $\chi^2_{\rm IP}$ of the π^+ and π^-, and the $\bar{B}^0$ properties of vertex χ^2, pointing angle, flight distance, $p_{\rm T}$ and $\chi^2_{\rm IP}$. The BDT is trained on a simulated sample of two million $\bar{B}^0 \to J/\psi\pi^+\pi^-$ signal events generated uniformly in phase space with unpolarized $J/\psi \to \mu^+\mu^-$ decays, and a background data sample from the sideband $5566 < m(J/\psi\pi^+\pi^-) < 5616$ MeV. Then the BDT is tested on independent samples from the same sources. The BDT can take any value from -1 to 1. The distributions of signal and background are approximately Gaussian shaped with a rms of about 0.13. The signal peaks at BDT of 0.27 and background at -0.22. To minimize possible bias on the signal acceptance due to the BDT, we choose a loose requirement of BDT > 0, which has about a 95% signal efficiency and a 90% background rejection rate.

V. FIT MODEL

We first select events based on their $J/\psi\pi^+\pi^-$ invariant mass and then perform a full fit to the decay variables. The invariant mass of the selected $J/\psi\pi^+\pi^-$ combinations is shown in Fig. 3. There is a large peak at the $\bar{B}^0_s$ mass and a smaller one at the $\bar{B}^0$ mass on top of the background. A double crystal ball function with common means models the radiative tails and is used to fit each of the signals [23].

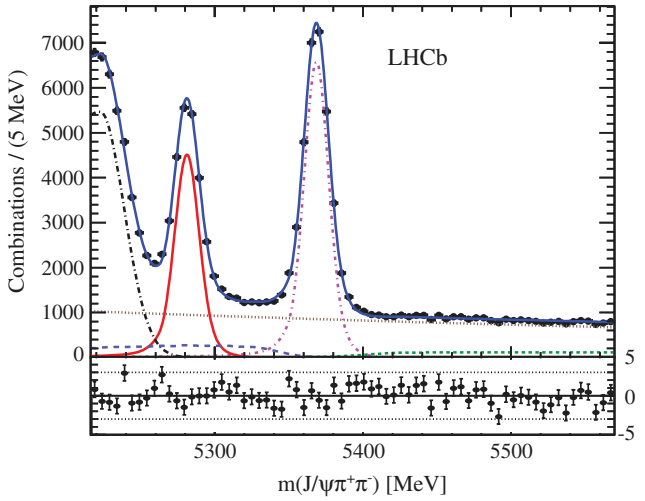

FIG. 3 (color online). Invariant mass of $J/\psi\pi^+\pi^-$ combinations together with the data fit. The (red) solid curve shows the $\bar{B}^0$ signal, the (brown) dotted line shows the combinatorial background, the (green) short-dashed line shows the B^- background, the (purple) dot-dashed curve is $\bar{B}^0_s \to J/\psi\pi^+\pi^-$, the (light blue) long-dashed line is the sum of $\bar{B}^0_s \to J/\psi\eta^{(\prime)}$, $\bar{B}^0_s \to J/\psi\phi$ with $\phi \to \pi^+\pi^-\pi^0$ backgrounds and the $\Lambda^0_b \to J/\psi K^- p$ reflection, the (black) dot-long dashed curve is the $\bar{B}^0 \to J/\psi K^-\pi^+$ reflection and the (blue) solid curve is the total. The points at the bottom show the difference between the data points and the total fit divided by the statistical uncertainty on the data.

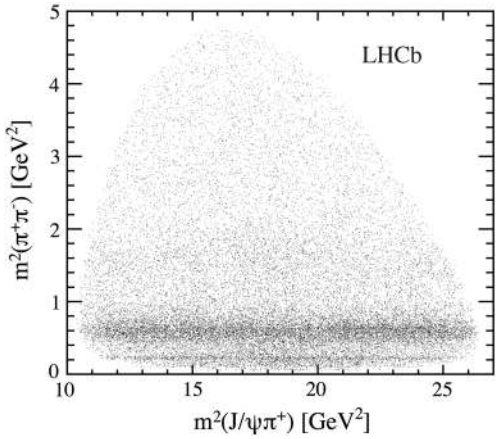

FIG. 4. Distribution of $m^2(\pi^+\pi^-)$ versus $m^2(J/\psi\pi^+)$ for all events within ± 20 MeV of the $\bar{B}^0$ mass.

The known $\bar{B}^0_s - \bar{B}^0$ mass difference [19] is used to constrain the difference in mean values. Other components in the fit model take into account background contributions from $B^- \to J/\psi K^-$ and $B^- \to J/\psi\pi^-$ decays combined with a random π^+, $\bar{B}^0_s \to J/\psi\eta(')$ with $\eta(') \to \pi^+\pi^-\gamma$, $\bar{B}^0_s \to J/\psi\phi$ with $\phi \to \pi^+\pi^-\pi^0$, $\bar{B}^0 \to J/\psi K^-\pi^+$ and $\Lambda^0_b \to J/\psi K^- p$ reflections, and combinatorial backgrounds. The exponential combinatorial background shape is taken from like-sign combinations, that are the sum of $\pi^+\pi^+$ and $\pi^-\pi^-$ candidates, and found to be a good description in previous studies [20,24].

The shapes of the other components are taken from the Monte Carlo simulation with their normalizations allowed to vary. The mass fit gives $18\,841 \pm 204$ signal and $10\,207 \pm 178$ background candidates within ± 20 MeV of the $\bar{B}^0$ mass peak. Only candidates within ± 20 MeV of the $\bar{B}^0$ mass peak are retained for further analysis. To improve the resolution of the mass and angular variables used in the amplitude analysis, we perform a kinematic fit constraining the $\bar{B}^0$ and J/ψ masses to their PDG mass values [19] and recompute the final state momenta [25].

One of the main challenges in performing a mass and angular analysis is to construct a realistic probability density function, where both the kinematic and dynamical properties are modeled accurately. The PDF is given by the sum of signal, S, and background, B, functions. The $\bar{B}^0$ signal includes events from the reaction $\bar{B}^0 \to J/\psi K^0_S$. These are described by a separate term in the PDF. The total PDF is

$$\begin{aligned} F(m_{hh},\theta_{hh},\theta_{J/\psi},\chi) &= f_{\rm sig}\left[\frac{1-f_{K^0_S}}{\mathcal{N}_{\rm sig}}\varepsilon(m_{hh},\theta_{hh},\theta_{J/\psi},\chi)S(m_{hh},\theta_{hh},\theta_{J/\psi},\chi)\right. \\ &\left. + \frac{f_{K^0_S}}{\mathcal{N}_{K^0_S}}\varepsilon(m_{hh},\theta_{hh},\theta_{J/\psi},\chi)G(m_{hh};m_{K^0_S},\sigma_{K^0_S})\sin^2\theta_{J/\psi}\right] \\ &+ (1-f_{\rm sig})B(m_{hh},\theta_{hh},\theta_{J/\psi},\chi), \end{aligned} \tag{15}$$

where $f_{\rm sig}$ is the fraction of the signal in the fitted region [$f_{\rm sig} = (64.9 \pm 1.2)\%$ obtained from the mass fit in Fig. 3], ε is the detection efficiency described in Sec. V A, and B is the background PDF described in Sec. V B. The K^0_S component is modeled by a Gaussian function, G, with mean $m_{K^0_S}$ and width $\sigma_{K^0_S}$. The Gaussian parameters together with the K^0_S fraction in the $\bar{B}^0$ peak, $f_{K^0_S}$, are determined in the fit. The normalization factors $\mathcal{N}_{\rm sig}$ for the signal and $\mathcal{N}_{K^0_S}$ for the K^0_S candidates are efficiency-multiplied theoretical functions integrated over the four analysis variables, m_{hh}, θ_{hh}, $\theta_{J/\psi}$ and χ, given by

$$\begin{aligned} \mathcal{N}_{\rm sig} = \int \varepsilon(m_{hh},\theta_{hh},\theta_{J/\psi},\chi)S(m_{hh},\theta_{hh},\theta_{J/\psi},\chi) \\ \times dm_{hh}d\cos\theta_{hh}d\cos\theta_{J/\psi}d\chi. \end{aligned} \tag{16}$$

Examination of the event distribution for $m^2(\pi^+\pi^-)$ versus $m^2(J/\psi\pi^+)$ in Fig. 4 shows obvious structures in $m^2(\pi^+\pi^-)$. To investigate if there are visible exotic structures in $m^2(J/\psi\pi^+)$, we examine the $J/\psi\pi^+$ invariant mass

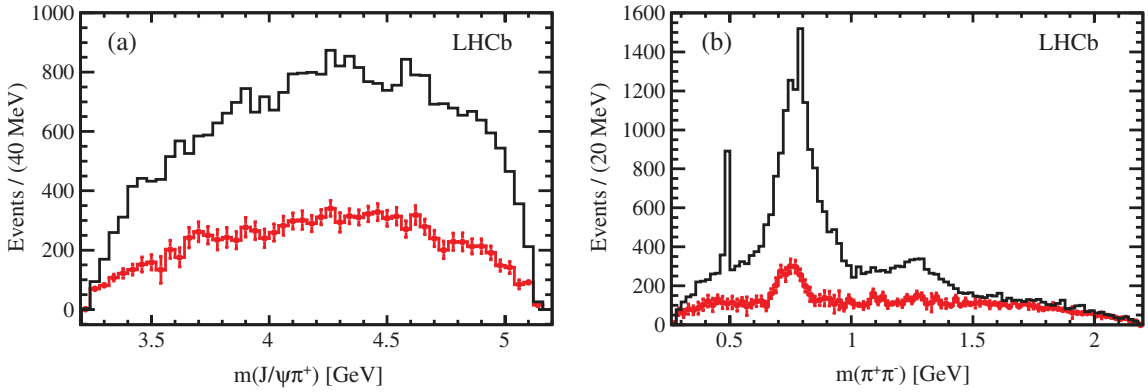

FIG. 5 (color online). Distributions of (a) $m(J/\psi\pi^+)$ and (b) $m(\pi^+\pi^-)$ for $\bar{B}^0 \to J/\psi\pi^+\pi^-$ candidates within ± 20 MeV of the $\bar{B}^0$ mass. The red points with error bars show the background contributions obtained by fitting the $m(J/\psi\pi^+\pi^-)$ distribution in bins of the plotted variables.

TABLE II. Efficiency parameters. There are substantial correlations.

ϵ_1	0.1220 ± 0.0097
ϵ_2	0.1163 ± 0.0182
ϵ_3	0.0051 ± 0.0004
ϵ_4	0.0399 ± 0.0101
ϵ_5	-0.0012 ± 0.0007
ϵ_6	0.10051 ± 0.0023
ϵ_7	0.0002 ± 0.0005
ϵ_8	-0.000150 ± 0.000007
ϵ_9	-0.000011 ± 0.000261
ϵ_{10}	0.000350 ± 0.000146
ϵ_{11}	-0.000113 ± 0.000011

distribution as shown in Fig. 5(a) where we fit the $m(J/\psi\pi^+\pi^-)$ distribution to extract the background levels in bins of $m(J/\psi\pi^+)$ (red points). Similarly, Fig. 5(b) shows the $\pi^+\pi^-$ mass distribution. Apart from a large signal peak due to the $\rho(770)$, there are visible structures at about 1270 MeV and a K^0_S component at about 500 MeV.

A. Detection efficiency

The detection efficiency is determined from a sample of about four million simulated $\bar{B}^0 \to J/\psi\pi^+\pi^-$ events that are generated uniformly in phase space with unpolarized $J/\psi \to \mu^+\mu^-$ decays. The efficiency model can be expressed as

$$\varepsilon(m_{hh}, \theta_{hh}, \theta_{J/\psi}, \chi) = \varepsilon_1(s_{12}, s_{13}) \times \varepsilon_2(\theta_{J/\psi}, m_{hh}) \times \varepsilon_3(\chi, m_{hh}), \quad (17)$$

where $s_{12} \equiv m^2(J/\psi\pi^+)$ and $s_{13} \equiv m^2(J/\psi\pi^-)$ are functions of (m_{hh}, θ_{hh}); such parameter transformations in ε_1 are implemented in order to use the Dalitz-plot based efficiency model developed in previous publications [4,20].

The efficiency dependence on χ is modeled by

$$\varepsilon_3(\chi, m_{hh}) = \frac{1}{2\pi}(1 + p_1 \cos\chi + p_2 \cos 2\chi), \quad (18)$$

where $p_1 = p_1^0 + p_1^1 \times m_{hh}^2$ and $p_2 = p_2^0 + p_2^1 \times m_{hh}^2 + p_2^2 \times m_{hh}^4$. The free parameters are determined by fitting the simulated χ distributions using Eq. (18) in bins of m_{hh}^2. The fit gives $p_1^0 = -0.0065 \pm 0.0052$ and $p_1^1 = (0.0011 \pm 0.0021)\,\text{GeV}^{-2}$; $p_2^0 = -0.0006 \pm 0.0079$, $p_2^1 = (0.0602 \pm 0.0083)\,\text{GeV}^{-2}$ and $p_2^2 = (-0.0099 \pm 0.0018)\,\text{GeV}^{-4}$.

The acceptance in $\cos\theta_{J/\psi}$ depends on m_{hh}. We disentangle this correlation by fitting the $\cos\theta_{J/\psi}$ distribution in 24 bins of m_{hh}^2 using the parametrization

$$\varepsilon_2(\theta_{J/\psi}, m_{hh}) = \frac{1 + a\cos^2\theta_{J/\psi}}{2 + 2a/3}. \quad (19)$$

The fitted values of a are modeled by a second order polynomial function,

$$a(m_{hh}^2) = a_0 + a_1 m_{hh}^2 + a_2 m_{hh}^4, \quad (20)$$

with $a_0 = 0.189 \pm 0.021$, $a_1 = -0.116 \pm 0.021\ \text{GeV}^{-2}$ and $a_2 = 0.017 \pm 0.004\ \text{GeV}^{-4}$.

We model the detection efficiency, $\varepsilon_1(s_{12}, s_{13})$, by using the symmetric observables

$$x = s_{12}/\text{GeV}^2 - 18.4, \quad \text{and} \quad y = s_{13}/\text{GeV}^2 - 18.4. \quad (21)$$

These variables are related to s_{23} by

$$s_{12} + s_{13} + s_{23} = m_B^2 + m_{J/\psi}^2 + m_{\pi^+}^2 + m_{\pi^-}^2. \quad (22)$$

Thus, $\varepsilon_1(s_{12}, s_{13})$ can be modeled by a two-dimensional fifth order polynomial function as

$$\begin{aligned}\varepsilon_1(s_{12}, s_{13}) = 1 &+ \epsilon_1(x+y) + \epsilon_2(x+y)^2 + \epsilon_3 xy \\ &+ \epsilon_4(x+y)^3 + \epsilon_5 xy(x+y) + \epsilon_6(x+y)^4 \\ &+ \epsilon_7 xy(x+y)^2 + \epsilon_8 x^2y^2 + \epsilon_9(x+y)^5 \\ &+ \epsilon_{10} xy(x+y)^3 + \epsilon_{11} x^2y^2(x+y), \end{aligned} \quad (23)$$

where all the ϵ_i are the fit parameters. The χ^2/ndf is 313/299. The values of the parameters are given in Table II.

The projections of the fit used to measure the efficiency parameters are shown in Fig. 6. The efficiency shapes are

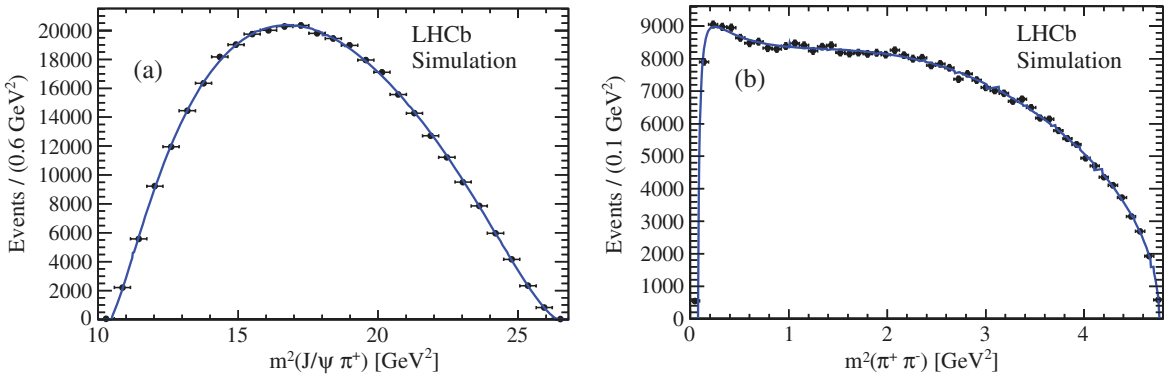

FIG. 6 (color online). Projections of invariant mass squared (a) $s_{12} \equiv m^2(J/\psi\pi^+)$ and (b) $s_{23} \equiv m^2(\pi^+\pi^-)$ of the simulated Dalitz plot used to measure the efficiency parameters. The points represent the simulated event distributions and the curves the polynomial fit.

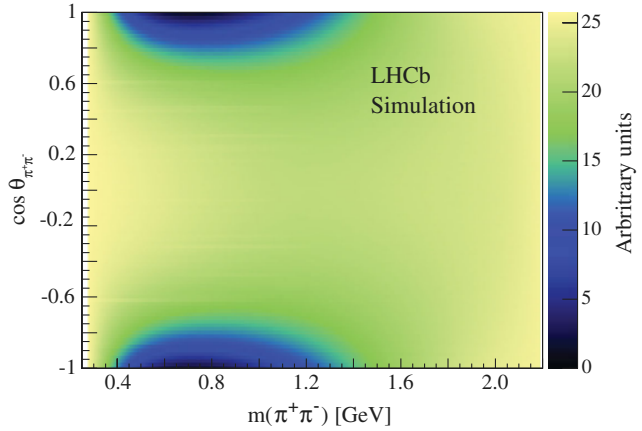

FIG. 7 (color online). The variation of ϵ_1 is shown as a function of $m(\pi^+\pi^-)$ and $\cos\theta_{\pi^+\pi^-}$.

well described by the parametrization. The parametrized efficiency as a function of $m(\pi^+\pi^-)$ versus $\cos\theta_{\pi^+\pi^-}$ is shown in Fig. 7.

B. BACKGROUND COMPOSITION

The main background source in the $\bar{B}^0$ signal region is combinatorial and can be taken from the like-sign combinations within ± 20 MeV of the $\bar{B}^0$ mass peak. In addition, there is background arising from partially reconstructed $\bar{B}^0_s$ decays ($\bar{B}^0_s \to J/\psi\eta(')$, with $\eta(') \to \pi^+\pi^-\gamma$ and $\bar{B}^0_s \to J/\psi\phi$ with $\phi \to \pi^+\pi^-\pi^0$), reflections from misidentified $\Lambda^0_b \to J/\psi K^- p$ and $\bar{B}^0 \to J/\psi K^-\pi^+$ decays, which cannot be present in the like-sign combinations. We use simulated samples of these decays to model their contributions. The Λ^0_b normalizations are determined from a previous analysis [26]. The background level in the opposite-sign combination ($\bar{B}^0 \to J/\psi\pi^+\pi^-$) is studied by fitting the $m(J/\psi\pi^+\pi^-)$ distributions in bins of $m(\pi^+\pi^-)$. The resulting background distribution in the ± 20 MeV $\bar{B}^0$ signal region is shown in Fig. 8 by points with error bars. A fit to this distribution gives a partially reconstructed $\bar{B}^0_s$ background fraction of 10.7%, the reflection from $\bar{B}^0$ of 5.3% and the reflection from the Λ^0_b baryon of 15.5% of the total background. The like-sign combinations summed with the additional backgrounds modeled by simulation are shown in Fig. 8.

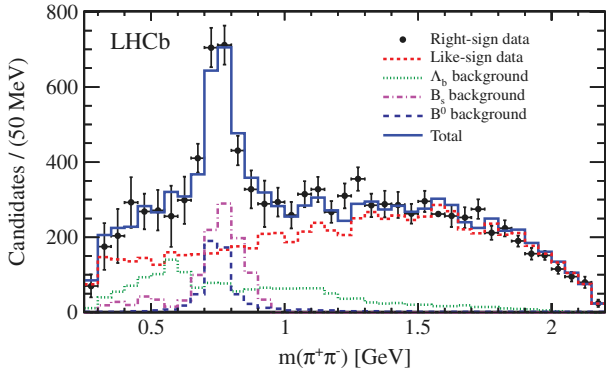

FIG. 8 (color online). Distributions of $m(\pi^+\pi^-)$ of background components. The (blue) histogram shows the like-sign combinations added with additional backgrounds using simulations. The (black) points with error bars show the background obtained from the fits to the $m(J/\psi\pi^+\pi^-)$ mass spectrum in each bin of $\pi^+\pi^-$ mass.

When this data-simulation hybrid sample is used to extract the background parameters, a further reweighting procedure is applied based on comparison of $m(\pi^+\pi^-)$ distributions between the overall fit and the background data points in Fig. 5(b).

To better model the angular distributions in the $\rho(770)$ mass region, the background is separated into the $\bar{K}^{*0}$ reflection from $\bar{B}^0$, the ρ, and other backgrounds. The total background PDF is the sum of these three components:

$$\begin{aligned} &B(m_{hh},\theta_{hh},\theta_{J/\psi},\chi) \\ &= \frac{f_{\bar{K}^{*0}}}{\mathcal{N}_{\bar{K}^{*0}}} B_{\bar{K}^{*0}}(m_{hh},\theta_{hh},\theta_{J/\psi},\chi) + \frac{f_\rho}{\mathcal{N}_\rho} B_\rho(m_{hh},\theta_{hh},\theta_{J/\psi},\chi) \\ &\quad + \frac{1-f_{\bar{K}^{*0}}-f_\rho}{\mathcal{N}_{\text{other}}} B_{\text{other}}(m_{hh},\theta_{hh},\theta_{J/\psi},\chi), \end{aligned} \tag{24}$$

where the $\mathcal{N}$s are normalizations, the contributing fractions having values of $f_{\bar{K}^{*0}} = (5.3 \pm 0.2)\%$ and $f_\rho = (9.5 \pm 0.6)\%$; the other background is normalized as $1 - f_{\bar{K}^{*0}} - f_\rho$.

The $\bar{K}^{*0}$ background is modeled by the function

$$\begin{aligned} &B_{\bar{K}^{*0}}(m_{hh},\theta_{hh},\theta_{J/\psi},\chi) \\ &= \left(\frac{p_R}{m_{hh}}\right)^2 \frac{m_{hh} e^{-a\cdot(1-|\cos\theta_{hh}|)}}{(m_0^2 - m_{hh}^2)^2 + m_0^2\Gamma_0^2} \times (1-|\cos\theta_{hh}|)^b \\ &\quad \times (1+\alpha_0\cos^2\theta_{J/\psi}) \times (1 + p_{b1}\cos\chi + p_{b2}\cos 2\chi), \end{aligned} \tag{25}$$

where m_0, Γ_0, a, b, α_0 are free parameters determined by fitting to the $\bar{B}^0 \to J/\psi\bar{K}^{*0}$ simulation. The last part $(1 + p_{b1}\cos\chi + p_{b2}\cos 2\chi)$ is a function of the χ angle. We have verified that the three backgrounds have consistent χ distributions; thus, the parameters p_{b1} and p_{b2} are determined by fitting all backgrounds simultaneously.

The ρ background is described by the function

$$\begin{aligned} &B_\rho(m_{hh},\theta_{hh},\theta_{J/\psi},\chi) \\ &= \left(\frac{p_R}{m_{hh}}\right)^2 \frac{m_{hh}}{(m_\rho^2 - m_{hh}^2)^2 + m_\rho^2\Gamma_\rho^2} \times \sin^2\theta_{hh} \\ &\quad \times \sin^2\theta_{J/\psi} \times (1 + p_{b1}\cos\chi + p_{b2}\cos 2\chi), \end{aligned} \tag{26}$$

where m_ρ, Γ_ρ are free parameters. The parameters are obtained by fitting to simulated $\bar{B}^0_s \to J/\psi\eta'(\to \rho\gamma)$ events.

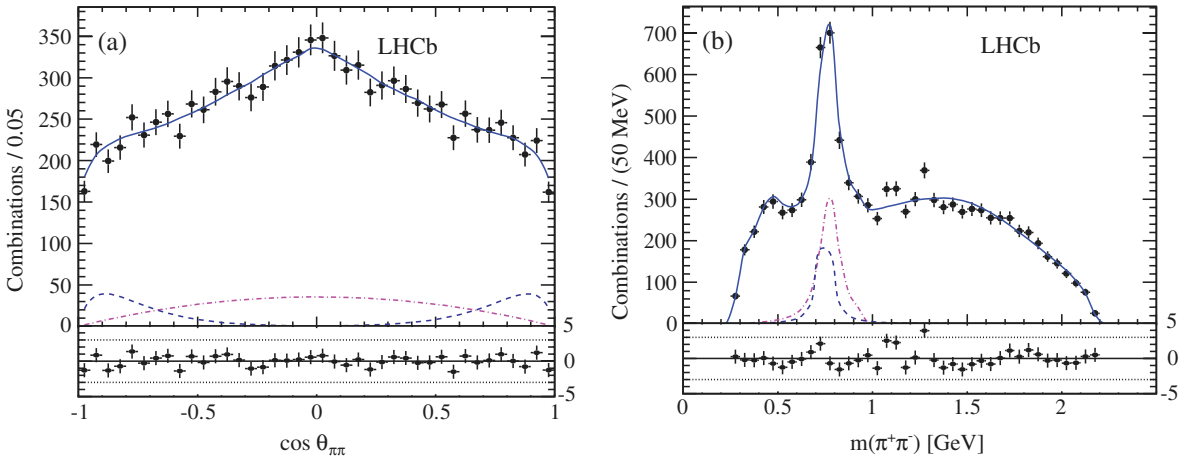

FIG. 9 (color online). Projections of (a) $\cos\theta_{\pi\pi}$ and (b) $m(\pi^+\pi^-)$ of the background. The points with error bars show the like-sign data combinations added with the Λ_b^0 background and additional simulated backgrounds. The (magenta) dot-dashed line shows the $\eta^{(\prime)} \to \rho\gamma$ background, the (dark-blue) dashed line the $\bar{K}^*$ reflection background, and the (blue) solid line the total. The points at the bottom show the difference between the data points and the total fit divided by the statistical uncertainty on the data.

The model for the remaining backgrounds is

$$B_{\rm other}(m_{hh},\theta_{hh},\theta_{J/\psi},\chi) = m_{hh}B_1(m_{hh}^2,\cos\theta_{hh}) \times (1+\alpha_1\cos^2\theta_{J/\psi}) \times (1+p_{b1}\cos\chi + p_{b2}\cos 2\chi), \quad (27)$$

with the function

$$B_1(m_{hh}^2,\cos\theta_{hh}) = \left[B_2(\zeta)\frac{p_B}{m_B} + \frac{b_0}{(m_1^2-m_{hh}^2)^2+m_1^2\Gamma_1^2}\right] \times \frac{1+q(\zeta)|\cos\theta_{hh}|+p(\zeta)\cos^2\theta_{hh}}{2[1+q(\zeta)/2+p(\zeta)/3]}. \quad (28)$$

Here the variable $\zeta = 2(m_{hh}^2 - m_{\rm min}^2)/(m_{\rm max}^2 - m_{\rm min}^2) - 1$, where $m_{\rm min}$ and $m_{\rm max}$ are the fit boundaries, $B_2(\zeta)$ is a fifth order Chebychev polynomial with coefficients b_i ($i = 1$–5), and $q(\zeta)$ and $p(\zeta)$ are two first order Chebychev polynomials with parameters c_j ($j = 1$–4).

Figure 9 shows the projections of $\cos\theta_{\pi\pi}$ and $m(\pi^+\pi^-)$ from the like-sign data combinations added with all the additional simulated backgrounds. The other background includes the Λ_b^0 background and the combinatorial background which is described by the like-sign combinations. The fitted background parameters are given in Table III. The $\cos\theta_{J/\psi}$ background distribution is shown in Fig. 10. Last, the χ background distribution, shown in the Fig. 11 fit with the function $1 + p_{b1}\cos\chi + p_{b2}\cos 2\chi$, determines the parameters $p_{b1} = -0.004 \pm 0.013$ and $p_{b2} = 0.070 \pm 0.013$.

TABLE III. Parameters for the background model.

m_0	0.7473 ± 0.0009 GeV
Γ_0	0.071 ± 0.02 GeV
m_1	0.45 ± 0.05 GeV
Γ_1	0.18 ± 0.05 GeV
m_ρ	0.770 ± 0.002 GeV
Γ_ρ	0.110 ± 0.004 GeV
a	6.94 ± 0.20
b	0.76 ± 0.04
b_0	0.0019 ± 0.0004 GeV^4
b_1	-0.536 ± 0.053
b_2	0.100 ± 0.043
b_3	-0.100 ± 0.042
b_4	0.080 ± 0.026
b_5	-0.051 ± 0.025
c_1	-0.048 ± 0.017
c_2	-0.172 ± 0.263
c_3	-0.142 ± 0.170
c_4	0.855 ± 0.259
α_0	0.45 ± 0.04
α_1	0.30 ± 0.03

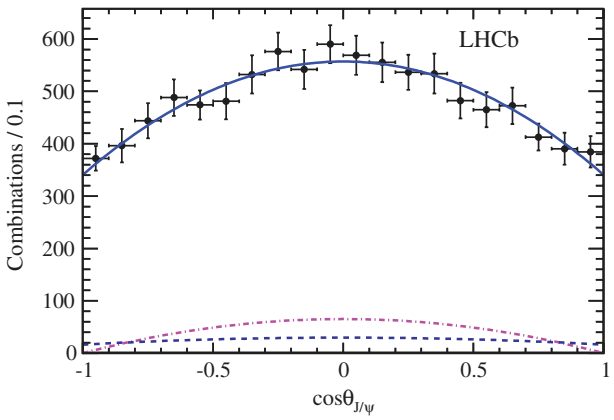

FIG. 10 (color online). The $\cos\theta_{J/\psi}$ distribution of the data-simulated hybrid background sample. The points with error bars show the like-sign data combinations added with the Λ_b^0 background and additional simulated backgrounds. The (magenta) dot-dashed line shows the ρ background, the (dark-blue) dashed the $\bar{K}^*$ reflection background and the (blue) solid line the total.

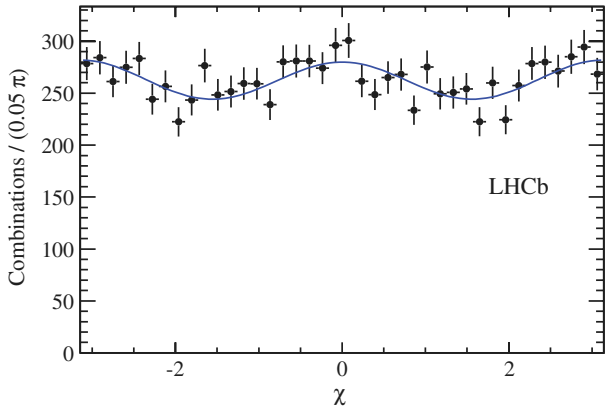

FIG. 11 (color online). The χ distribution of the data-simulated hybrid background sample including the Λ_b^0 background and the fitted function $1 + p_{b1}\cos\chi + p_{b2}\cos 2\chi$. The p-value of this fit is 40%.

C. RESONANCE MODELS

To study the resonant structures of the decay $\bar{B}^0 \to J/\psi\pi^+\pi^-$ we use 29 047 event candidates with invariant mass within ± 20 MeV of the $\bar{B}^0$ mass peak which include 10207 ± 178 background candidates. The background yield is fixed in the fit. Apart from nonresonant (NR) decays, the possible resonance candidates in the decay $\bar{B}^0 \to J/\psi\pi^+\pi^-$ are listed in Table IV. We use Breit-Wigner (BW) functions for most of the resonances except $f_0(980)$. The masses and widths of the BW resonances are listed in Table IV. When used in the fit, they are fixed to these values except for the parameters of $f_0(500)$ which are allowed to vary by their uncertainties. For the $f_0(980)$ we use a Flatté shape [27]. Besides the mass, this shape has two additional parameters, $g_{\pi\pi}$ and g_{KK}, which are fixed in the fit to the ones obtained from an amplitude analysis of $\bar{B}_s^0 \to J/\psi\pi^+\pi^-$ [28], where a large signal is evident. These parameters are $m_0 = 945.4 \pm 2.2$ MeV, $g_{\pi\pi} = 167 \pm 7$ MeV and $g_{KK}/g_{\pi\pi} = 3.47 \pm 0.12$. All background and efficiency parameters are fixed in the fit.

To determine the complex amplitudes in a specific model, the data are fitted maximizing the unbinned likelihood given as

$$\mathcal{L} = \prod_{i=1}^{N} F(m_{hh}^i, \theta_{hh}^i, \theta_{J/\psi}^i, \chi^i), \tag{29}$$

where N is the total number of candidates, and F is the total PDF defined in Eq. (15).

VI. FIT RESULTS

A. Final state composition

In order to compare the different models quantitatively, an estimate of the goodness of fit is calculated from four-dimensional partitions of the fitting variables. To distinguish between models, we use the Poisson likelihood χ^2 [30] defined as

$$\chi^2 = 2\sum_{i=1}^{N_{\rm bin}} \left[x_i - n_i + n_i \ln\left(\frac{n_i}{x_i}\right)\right], \tag{30}$$

where n_i is the number of events in the four-dimensional bin i and x_i is the expected number of events in that bin

TABLE IV. Possible resonance candidates in the $\bar{B}^0 \to J/\psi\pi^+\pi^-$ decay mode.

Resonance	Spin	Helicity	Resonance formalism	Mass (MeV)	Width (MeV)	Source
$\rho(770)$	1	$0, \pm 1$	BW	775.49 ± 0.34	149.1 ± 0.8	PDG [19]
$f_0(500)$	0	0	BW	513 ± 32	335 ± 67	CLEO [29]
$f_2(1270)$	2	$0, \pm 1$	BW	1275.1 ± 1.2	$185.1^{+2.9}_{-2.4}$	PDG [19]
$\omega(782)$	1	$0, \pm 1$	BW	782.65 ± 0.12	8.49 ± 0.08	PDG [19]
$f_0(980)$	0	0	Flatté	–	–	See text
$\rho(1450)$	1	$0, \pm 1$	BW	1465 ± 25	400 ± 60	PDG [19]
$\rho(1700)$	1	$0, \pm 1$	BW	1720 ± 20	250 ± 100	PDG [19]
$f_0(1500)$	0	0	BW	1461 ± 3	124 ± 7	LHCb [28]
$f_0(1710)$	0	0	BW	1720 ± 6	135 ± 8	PDG [19]

TABLE V. The χ^2/ndf and the $-\ln\mathcal{L}$ of different resonance models. The decrease of $-\ln\mathcal{L}$ is with respect to the 5R model.

Resonance model	$-\ln\mathcal{L}$	χ^2/ndf	Decrease of $-\ln\mathcal{L}$
5R model	−169271	2396/2041	
5R model + $\rho(1700)$ (best model)	−169327	2293/2035	56
Best model + $f_0(980)$ (7R model)	−169329	2295/2033	58
7R + $f_0(1500)$	−169333	2293/2031	60
7R + $f_0(1710)$	−169329	2295/2031	56
7R + NR	−169342	2292/2031	69

according to the fitted likelihood function. The χ^2/ndf and the negative of the logarithm of the likelihood, $-\ln\mathcal{L}$, of the fits are given in Table V for various fitting models, where ndf, the number of degrees of freedom, is equal to $N_{\rm bin}$ minus the number of fit parameters minus one. Here the five-resonance (5R) model contains the resonances $\rho(770)$, $f_0(500)$, $f_2(1270)$, $\rho(1450)$ and $\omega(782)$; the "best model" adds a $\rho(1700)$ resonance to the 5R model, the seven-resonance (7R) model adds a $f_0(980)$ resonance to the best model, and the 7R + NR model adds a nonresonant component. We also give the change of $-\ln\mathcal{L}$ for various fits with respect to the 5R model in Table V.

The 7R model gives a slightly better likelihood compared to the best model; however, the decrease of the $-\ln\mathcal{L}$ due to adding $f_0(980)$ is less than the expected $-\ln\mathcal{L}$ at 3σ significance. Thus, we use the best model, which maintains a significance larger than 3σ for each resonance component, as our baseline fit, while the 7R model is only used to establish an upper limit on the presence of the $f_0(980)$. The Dalitz fit projections on the four observables: $m(\pi^+\pi^-)$, $\cos(\theta_{\pi^+\pi^-})$, $\cos\theta_{J/\psi}$ and χ are shown in Fig. 12 for the best model.

Table VI shows the summary of fit fractions of different components for various models. The fit fractions of the interference terms in the best model are computed using Eq. (13) and listed in Table VII. Table VIII shows the resonant phases from the best model. In the best model the *CP* even components sum to $(56.0 \pm 1.4)\%$, including the interference terms, so that the *CP* odd fraction is $(44.0 \pm 1.4)\%$. The structure near the peak of the $\rho(770)$ is due to $\rho-\omega$ interference. The fit fraction ratio is found to be

$$\frac{\Gamma(\bar{B}^0 \to J/\psi\omega(782), \omega \to \pi^+\pi^-)}{\Gamma(\bar{B}^0 \to J/\psi\rho(770), \rho \to \pi^+\pi^-)} = (1.07^{+0.32+0.29}_{-0.22-0.22}) \times 10^{-2},$$

where the uncertainties are statistical and systematic, respectively; wherever two uncertainties are quoted in this paper, they will be of this form. The systematic uncertainties will be discussed in detail in Sec. VI C.

The 7R model fit gives the ratio of observed decays into $\pi^+\pi^-$ for $f_0(980)/f_0(500)$ equal to $(0.6^{+0.7+3.3}_{-0.4-2.6}) \times 10^{-2}$. To determine the statistical uncertainty, the full error matrix and parameter values from the fit are used to generate 500 data-size sample parameter sets. For each set, the fit fractions are calculated. The distributions of the obtained fit fractions are described by bifurcated Gaussian functions.

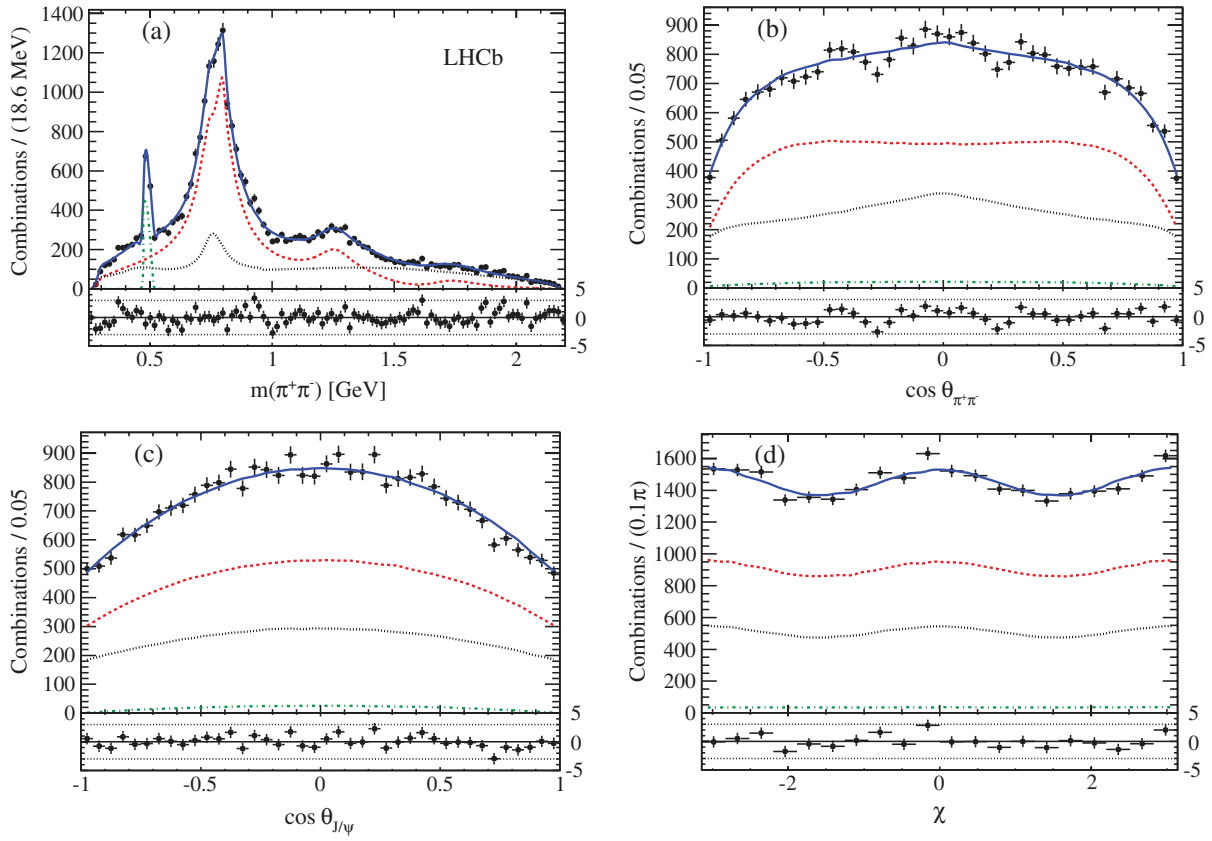

FIG. 12 (color online). Dalitz fit projections of (a) $m(\pi^+\pi^-)$, (b) $\cos(\theta_{\pi^+\pi^-})$, (c) $\cos\theta_{J/\psi}$ and (d) χ for the 5R model + $\rho(1700)$ (best model). The points with error bars are data compared with the overall fit, shown by the (blue) solid line. The individual fit components are signal, shown with a (red) dashed line, background, shown with a (black) dotted line and K^0_S, shown with a (green) dashed line.

TABLE VI. Fit fractions (%) of contributing components for the various models. The uncertainties are statistical only. Sums can differ from 100% due to interference (see Table VII).

	5R	Best Model	7R	7R + $f_0(1500)$	7R + $f_0(1710)$	7R + NR
$\rho(770)_0$	35.5 ± 1.6	36.2 ± 1.8	36.1 ± 1.8	36.1 ± 1.9	36.1 ± 1.8	36.0 ± 1.9
$\rho(770)_\parallel$	13.4 ± 1.1	14.7 ± 1.2	14.8 ± 1.2	14.7 ± 1.2	14.8 ± 1.2	14.9 ± 1.1
$\rho(770)_\perp$	11.7 ± 0.9	12.1 ± 1.1	11.9 ± 1.1	12.0 ± 1.1	12.0 ± 1.1	15.0 ± 1.3
$f_0(500)$	24.9 ± 1.4	22.2 ± 1.2	21.4 ± 1.7	20.8 ± 1.9	21.1 ± 1.8	18.7 ± 3.1
$f_2(1270)_0$	4.6 ± 0.4	4.7 ± 0.4	5.0 ± 0.4	4.8 ± 0.4	4.9 ± 0.4	4.5 ± 0.4
$f_2(1270)_\parallel$	1.0 ± 0.4	0.9 ± 0.4	1.0 ± 0.5	1.0 ± 0.5	1.0 ± 0.4	0.8 ± 0.4
$f_2(1270)_\perp$	2.1 ± 0.4	2.0 ± 0.4	2.0 ± 0.4	1.9 ± 0.4	2.0 ± 0.5	2.2 ± 0.4
$\omega(782)_0$	0.29 ± 0.11	0.26 ± 0.10	0.26 ± 0.11	0.26 ± 0.11	0.26 ± 0.11	0.25 ± 0.11
$\omega(782)_\parallel$	0.41 ± 0.15	0.41 ± 0.16	0.41 ± 0.16	0.42 ± 0.16	0.41 ± 0.15	0.39 ± 0.15
$\omega(782)_\perp$	$0.01^{+0.06}_{-0.01}$	$0.01^{+0.06}_{-0.01}$	$0.01^{+0.05}_{-0.01}$	$0.01^{+0.05}_{-0.01}$	$0.01^{+0.05}_{-0.01}$	$0.01^{+0.05}_{-0.01}$
$f_0(980)$	...	...	0.13 ± 0.11	0.16 ± 0.12	0.14 ± 0.11	0.5 ± 0.3
$\rho(1450)_0$	2.5 ± 0.6	6.8 ± 2.0	6.2 ± 2.4	5.3 ± 3.5	6.3 ± 2.3	5.0 ± 1.9
$\rho(1450)_\parallel$	1.8 ± 0.8	3.1 ± 1.9	3.2 ± 1.9	2.4 ± 0.8	3.4 ± 2.1	2.7 ± 1.7
$\rho(1450)_\perp$	1.6 ± 0.4	1.7 ± 0.7	1.8 ± 0.7	1.5 ± 0.7	1.9 ± 0.8	5.8 ± 2.6
$f_0(1500)$	...	...	...	$0.33^{+0.31}_{-0.18}$	...	...
$f_0(1710)$	...	...	...	...	$0.01^{+0.12}_{-0.01}$	...
$\rho(1700)_0$	...	2.0 ± 0.9	1.9 ± 1.0	$1.4^{+1.8}_{-0.8}$	2.0 ± 1.0	1.1 ± 0.7
$\rho(1700)_\parallel$	...	$1.2^{+1.2}_{-0.6}$	$1.3^{+1.1}_{-0.6}$	$1.3^{+1.3}_{-0.7}$	1.3 ± 1.0	1.0 ± 0.9
$\rho(1700)_\perp$	...	1.8 ± 0.7	1.7 ± 0.6	1.7 ± 0.6	1.8 ± 0.7	3.5 ± 1.2
NR	...	...	...	...	...	3.2 ± 1.1
Sum	99.8	110.2	108.8	105.9	109.3	115.5

The widths of the Gaussians are taken as the statistical errors on the corresponding parameters. We will discuss the implications of this measurement in Sec. VII.

In Fig. 13 we show the fit fractions of the different resonant components in the best model. Table IX lists the fit fractions and the transversity fractions of each contributing resonance. For a *P*- or *D*-wave resonance, we report its total fit fraction by summing all of the three components.

TABLE VII. Nonzero interference fractions (%) obtained from the fit using the best model. The uncertainties are statistical only.

Interfering components	Interference fraction (%)
$\rho(770)_0 + \omega(782)_0$	-0.36 ± 0.55
$\rho(770)_\parallel + \omega(782)_\parallel$	0.65 ± 0.43
$\rho(770)_\perp + \omega(782)_\perp$	-0.21 ± 0.37
$\rho(770)_0 + \rho(1450)_0$	-3.34 ± 2.60
$\rho(770)_\parallel + \rho(1450)_\parallel$	-4.38 ± 1.64
$\rho(770)_\perp + \rho(1450)_\perp$	-0.18 ± 1.21
$\rho(770)_0 + \rho(1700)_0$	3.34 ± 0.93
$\rho(770)_\parallel + \rho(1700)_\parallel$	0.63 ± 0.88
$\rho(770)_\perp + \rho(1700)_\perp$	2.10 ± 0.43
$\omega(782)_0 + \rho(1450)_0$	-0.24 ± 0.06
$\omega(782)_\parallel + \rho(1450)_\parallel$	-0.17 ± 0.06
$\omega(782)_\perp + \rho(1450)_\perp$	-0.02 ± 0.03
$\omega(782)_0 + \rho(1700)_0$	0.05 ± 0.03
$\omega(782)_\parallel + \rho(1700)_\parallel$	-0.05 ± 0.03
$\omega(782)_\perp + \rho(1700)_\perp$	-0.01 ± 0.02
$\rho(1450)_0 + \rho(1700)_0$	-5.57 ± 1.98
$\rho(1450)_\parallel + \rho(1700)_\parallel$	$-1.31^{+1.10}_{-2.89}$
$\rho(1450)_\perp + \rho(1700)_\perp$	-1.09 ± 1.02

Table X shows the branching fractions of the resonant modes calculated by multiplying the fit fraction listed in Table IX with $\mathcal{B}(\bar{B}^0 \to J/\psi\pi^+\pi^-) = (3.97 \pm 0.09 \pm 0.11 \pm 0.16) \times 10^{-5}$, obtained from our previous study [4], where the uncertainties are statistical, systematic, and due to normalization, respectively. These branching fractions are proportional to the squares of the individual resonant amplitudes.

TABLE VIII. The fitted resonant phases from the best model. The uncertainties are statistical only.

Components	Phase (°)
$\rho(770)_0$	0 (fixed)
$\rho(770)_\perp$	0 (fixed)
$\rho(770)_\parallel$	189.8 ± 7.3
$f_0(500)$	336.9 ± 5.0
$f_2(1270)_0$	210.1 ± 6.9
$f_2(1270)_\perp$	165.0 ± 13.3
$f_2(1270)_\parallel$	334.4 ± 21.9
$\omega(782)_0$	268.8 ± 11.9
$\omega(782)_\perp$	227.4 ± 84.9
$\omega(782)_\parallel$	123.5 ± 13.7
$\rho(1450)_0$	196.7 ± 12.1
$\rho(1450)_\perp$	182.6 ± 22.4
$\rho(1450)_\parallel$	74.9 ± 12.6
$\rho(1700)_0$	71.1 ± 19.9
$\rho(1700)_\perp$	113.4 ± 20.3
$\rho(1700)_\parallel$	3.4 ± 24.5

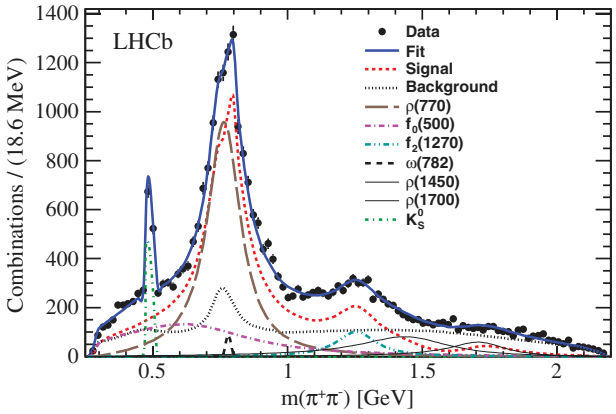

FIG. 13 (color online). Fit projection of $m(\pi^+\pi^-)$ showing the different resonant contributions in the best model.

B. ANGULAR MOMENTS

Angular moments are defined as an average of the spherical harmonics, $\langle Y_l^0(\cos\theta_{\pi\pi})\rangle$, in each efficiency-corrected and background-subtracted $\pi^+\pi^-$ invariant mass interval. The moment distributions provide an additional way of visualizing the effects of different resonances and their interferences, similar to a partial wave analysis. Figure 14 shows the distributions of the angular moments for the best model. In general the interpretation of these moments is that $\langle Y_0^0\rangle$ is the efficiency-corrected and background-subtracted event distribution, $\langle Y_1^0\rangle$ the sum of the interference between S-wave and P-wave and between P-wave and D-wave amplitudes, $\langle Y_2^0\rangle$ the sum of the P wave, D wave and the interference of S-wave and D-wave amplitudes, $\langle Y_3^0\rangle$ the interference between P wave and D wave, $\langle Y_4^0\rangle$ the D wave, and $\langle Y_5^0\rangle$ results from an F wave [20,31]. For the moments with odd-l, one will always find that $\bar{B}^0$ and B^0 have opposite signs; thus, the sum of their contributions is expected to be small.

C. Systematic uncertainties

The sources of systematic uncertainties on the results of the amplitude analysis are summarized in Table XI. Uncertainties due to particle identification and tracking are taken from Ref. [4] and are taken into account in the branching fraction results, but do not appear in the fit fractions as they are independent of pion kinematics. For the uncertainties due to the acceptance or background modeling, we repeat the data fit 100 times where the parameters of acceptance or background modeling are varied according to the corresponding error matrix. For the acceptance function, the error matrix is obtained by fitting the simulated acceptance as described in Sec. V A. For the background function, the error matrix is obtained by fitting the hybrid data-simulated sample as described in Sec. V B.

There is uncertainty on the fractions of sources in the hybrid MC-data sample for background modeling. Instead of using the fits to the $\pi^+\pi^-$ mass distribution to determine the background fractions, we use the fractions found from the $J/\psi\pi^+\pi^-$ mass fit shown in Fig. 3 that finds that the Λ_b^0 reflection is 9.6%, the $\bar{B}^0$ reflection is 4.2%, the $\bar{B}_s^0$ background is 11.5% and the combinatorial part is 74.7%, instead of the ones found in Sec. V B. We then fit the new hybrid sample to get the background parameters. The data fit is repeated with the new background parameters; the changes on the fit results are added in quadrature with the uncertainties of the background modeling discussed above. The two background uncertainties have similar sizes.

We neglect the mass resolution in the fit where the typical resolution is 3 MeV. A previous study shows that the resolution effects are negligible except for the $\omega(782)$ resonance whose total fit fraction is underestimated by $(0.09 \pm 0.08)\%$. We take the quadrature of 0.09% and 0.08%, equal to 0.12%, as the systematic uncertainty of the total fit fraction of the $\omega(782)$. These uncertainties are included in the "acceptance" category.

The uncertainties due to the fit model include adding each resonance that is listed in Table IV but not used in the 7R model, varying the centrifugal barrier factors defined in Eq. (5) substantially, replacing the $f_0(500)$ model by a Bugg function [32] and using the alternative Gounaris and Sakurai model [33] for the various ρ mesons. The largest variation among those changes is

TABLE IX. Fit fractions and transversity fractions of contributing resonances in the best model. The first uncertainty is statistical and the second the total systematic.

Component	Fit fraction (%)	Transversity fractions (%) $\tau = 0$	$\tau = \parallel$	$\tau = \perp$
$\rho(770)$	$63.1 \pm 2.2^{+3.4}_{-2.2}$	$57.4 \pm 2.0^{+1.3}_{-3.1}$	$23.4 \pm 1.7^{+1.0}_{-1.3}$	$19.2 \pm 1.7^{+3.8}_{-1.2}$
$f_0(500)$	$22.2 \pm 1.2^{+2.6}_{-3.5}$	1	0	0
$f_2(1270)$	$7.5 \pm 0.6^{+0.4}_{-0.6}$	$62 \pm 4^{+2}_{-4}$	$11 \pm 5 \pm 2$	$26 \pm 5^{+4}_{-2}$
$\omega(782)$	$0.68^{+0.20+0.17}_{-0.14-0.13}$	39^{+15+4}_{-13-3}	60^{+12+3}_{-15-4}	$1^{+9}_{-1} \pm 1$
$\rho(1450)$	$11.6 \pm 2.8 \pm 4.7$	$58 \pm 10^{+14}_{-23}$	$27 \pm 13^{+7}_{-11}$	$15 \pm 7^{+28}_{-10}$
$\rho(1700)$	$5.1 \pm 1.2 \pm 3.0$	$40 \pm 11^{+13}_{-23}$	$24 \pm 14^{+7}_{-10}$	$36 \pm 14^{+28}_{-9}$

TABLE X. Branching fractions for each channel. The first uncertainty is statistical and the second the total systematic.

R	$\mathcal{B}(\bar{B}^0 \to J/\psi R, R \to \pi^+\pi^-)$
$\rho(770)$	$(2.50 \pm 0.10^{+0.18}_{-0.15}) \times 10^{-5}$
$f_0(500)$	$(8.8 \pm 0.5^{+1.1}_{-1.5}) \times 10^{-6}$
$f_2(1270)$	$(3.0 \pm 0.3^{+0.2}_{-0.3}) \times 10^{-6}$
$\omega(782)$	$(2.7^{+0.8+0.7}_{-0.6-0.5}) \times 10^{-7}$
$\rho(1450)$	$(4.6 \pm 1.1 \pm 1.9) \times 10^{-6}$
$\rho(1700)$	$(2.0 \pm 0.5 \pm 1.2) \times 10^{-6}$

assigned as the systematic uncertainty for modeling. We also find that increasing the default angular momentum L_B for the P- and D-wave cases gives negligible differences.

Finally, we repeat the amplitude fit by varying the mass and width of all the resonances except for the $f_0(980)$, in the 7R model within their errors one at a time, and add the changes in quadrature. For the $f_0(980)$ resonance, we change the resonance parameters m_0, $g_{\pi\pi}$ and $g_{KK}/g_{\pi\pi}$ to the values obtained from solution II in [28] instead of using the ones obtained from solution I.

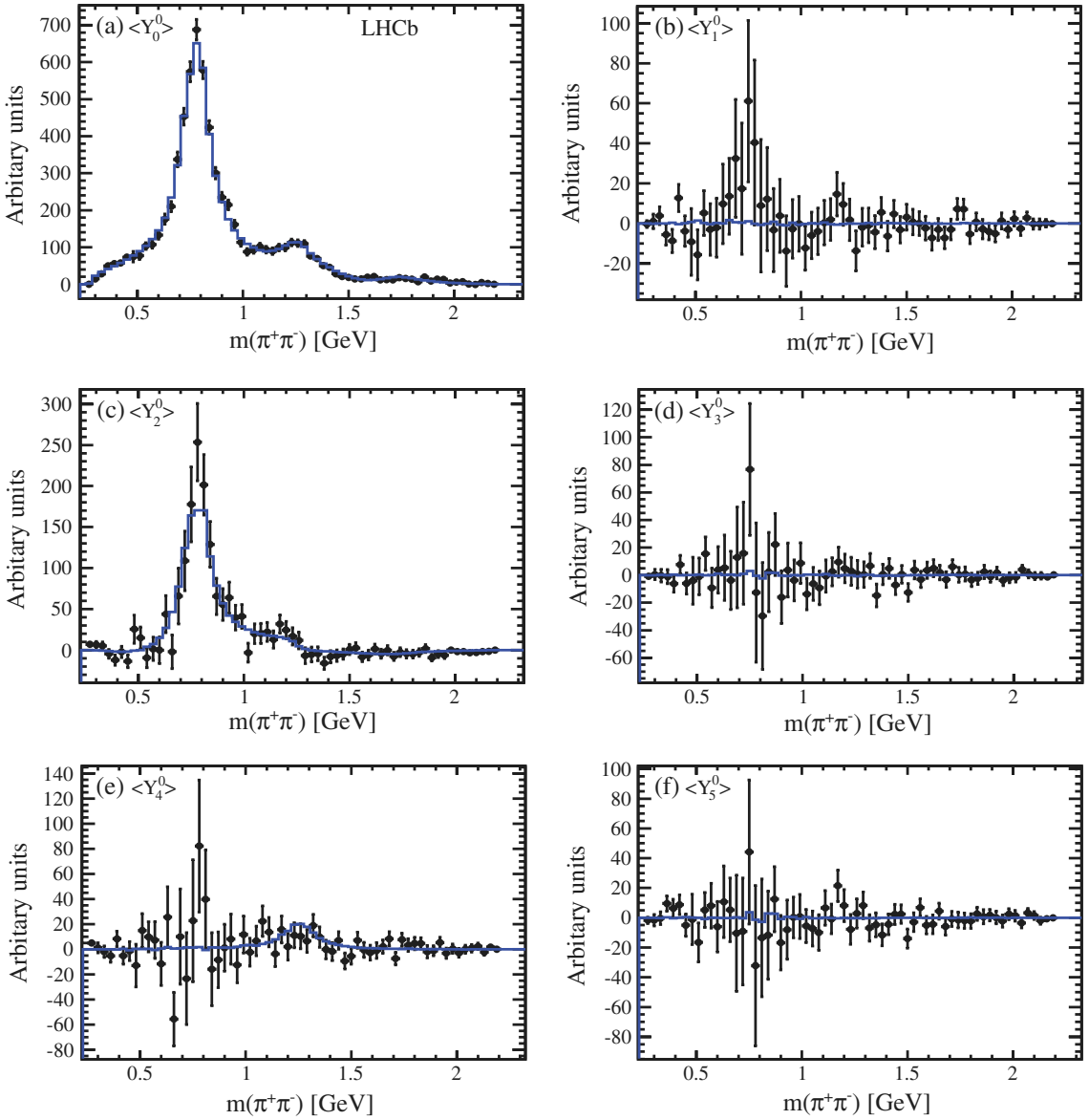

FIG. 14 (color online). The $\pi^+\pi^-$ mass dependence of the spherical harmonic moments of $\cos\theta_{\pi\pi}$ after efficiency corrections and background subtraction: (a) $\langle Y_0^0 \rangle$, (b) $\langle Y_1^0 \rangle$, (c) $\langle Y_2^0 \rangle$, (d) $\langle Y_3^0 \rangle$, (e) $\langle Y_4^0 \rangle$, (f) $\langle Y_5^0 \rangle$. The errors on the black data points are statistical. The (blue) curves show the fit projections.

TABLE XI. Absolute systematic uncertainties on the results of the amplitude analysis estimated using the best model except for the $f_0(980)$ where we use the 7R model.

Item	Acceptance	Background model	Fit model	Resonance parameters	Total
Fit fractions (%)					
$\rho(770)$	±0.3	±0.6	$^{+3.2}_{-1.8}$	±1.1	$^{+3.4}_{-2.2}$
$f_0(500)$	±0.3	±0.7	$^{+1.2}_{-2.7}$	±2.2	$^{+2.6}_{-3.5}$
$f_2(1270)$	±0.1	±0.2	$^{+0.1}_{-0.5}$	±0.3	$^{+0.4}_{-0.6}$
$\omega(782)$	±0.12	±0.02	$^{+0.11}_{-0.03}$	±0.03	$^{+0.17}_{-0.13}$
$f_0(980)$	±0.01	$^{+0.03}_{-0.02}$	$^{+0.37}_{-0.04}$	±0.03	$^{+0.37}_{-0.05}$
$\rho(1450)$	±0.15	±1.3	$^{+2.3}_{-1.9}$	±4.0	±4.7
$\rho(1700)$	±0.13	±0.7	$^{+0.7}_{-0.9}$	±2.9	±3.0
Transversity 0 fractions (%)					
$\rho(770)$	±0.5	±0.5	$^{+1.0}_{-3.0}$	±0.5	$^{+1.3}_{-3.1}$
$f_2(1270)$	±0.5	±1.7	$^{+0.8}_{-2.9}$	±1.0	$^{+2}_{-4}$
$\omega(782)$	±0.4	±2.1	$^{+3.5}_{-0.6}$	±1.5	$^{+4}_{-3}$
$\rho(1450)$	±0.7	±8.2	$^{+2.0}_{-18.4}$	±11.1	$^{+14}_{-23}$
$\rho(1700)$	±0.6	±9.9	$^{+0.4}_{-18.3}$	±8.7	$^{+13}_{-23}$
Transversity ‖ fractions (%)					
$\rho(770)$	±0.3	±0.5	$^{+0.1}_{-0.8}$	±0.8	$^{+1.0}_{-1.3}$
$f_2(1270)$	±0.4	±1.0	$^{+1.3}_{-1.4}$	±1.3	$^{+2}_{-2}$
$\omega(782)$	±0.4	±2.0	$^{+0.6}_{-3.3}$	±1.5	$^{+3}_{-4}$
$\rho(1450)$	±0.6	±5.1	$^{+3.0}_{-8.4}$	±4.4	$^{+7}_{-11}$
$\rho(1700)$	±1.0	±4.2	$^{+3.3}_{-7.9}$	±4.0	$^{+7}_{-10}$
Transversity ⊥ fractions (%)					
$\rho(770)$	±0.3	±0.3	$^{+3.8}_{-0.9}$	±0.6	$^{+3.8}_{-1.2}$
$f_2(1270)$	±0.3	±0.9	$^{+4.3}_{-1.9}$	±0.7	$^{+4}_{-2}$
$\omega(782)$	±0.1	±0.2	$^{+0.1}_{-0.2}$	±0.4	±0.5
$\rho(1450)$	±0.6	±3.4	$^{+26.8}_{-0.0}$	±9.3	$^{+29}_{-10}$
$\rho(1700)$	±0.7	±6.2	$^{+26.2}_{-0.0}$	±5.9	$^{+28}_{-9}$
Ratio of fit fractions (%)					
$f_0(980)/f_0(500)$	±0.09	±0.17	$^{+2.1}_{-0.1}$	±2.6	$^{+3.3}_{-2.6}$
$\omega(782)/\rho(770)$	±0.19	±0.04	$^{+0.21}_{-0.10}$	±0.05	$^{+0.29}_{-0.22}$

VII. SUBSTRUCTURE OF THE $f_0(980)$ AND $f_0(500)$ MESONS

The substructure of mesons belonging to the scalar nonet is controversial. Most mesons are thought to be formed from a combination of a q and a $\bar{q}$. Some authors introduce the concept of $q\bar{q}q\bar{q}$ states or superpositions of the tetraquark state with the $q\bar{q}$ state [34]. In either case, the $I=0$ $f_0(500)$ and the $f_0(980)$ are thought to be mixtures of the underlying states whose mixing angle has been estimated previously. In the $q\bar{q}$ model, the mixing is parametrized by a normal 2×2 rotation matrix characterized by the angle φ_m, so that the observed states are given in terms of the base states as

$$\begin{aligned}|f_0(980)\rangle &= \cos\varphi_m|s\bar{s}\rangle + \sin\varphi_m|n\bar{n}\rangle\\ |f_0(500)\rangle &= -\sin\varphi_m|s\bar{s}\rangle + \cos\varphi_m|n\bar{n}\rangle,\\ \text{where}|n\bar{n}\rangle &\equiv \frac{1}{\sqrt{2}}(|u\bar{u}\rangle + |d\bar{d}\rangle).\end{aligned} \tag{31}$$

In this case only the $|d\bar{d}\rangle$ part of the $|n\bar{n}\rangle$ wave function contributes (see Fig. 1). Thus, we have

$$\tan^2\varphi_m \equiv r_\sigma^f = \frac{\mathcal{B}(\bar{B}^0\to J/\psi f_0(980))}{\mathcal{B}(\bar{B}^0\to J/\psi f_0(500))}\frac{\Phi(500)}{\Phi(980)}, \tag{32}$$

where the Φ's are phase space factors [2,34,35]. The phase space in this pseudoscalar to vector-pseudoscalar decay is

proportional to the cube of the f_0 momenta. Taking the average of the momentum dependent phase space over the resonant line shapes results in the ratio of phase space factors $\frac{\Phi(500)}{\Phi(980)} = 1.25$.

The 7R model fit gives the ratio of branching fractions:

$$\frac{\mathcal{B}(\bar{B}^0 \to J/\psi f_0(980), f_0(980) \to \pi^+\pi^-)}{\mathcal{B}(\bar{B}^0 \to J/\psi f_0(500), f_0(500) \to \pi^+\pi^-)} = (0.6^{+0.7+3.3}_{-0.4-2.6}) \times 10^{-2}.$$

We need to correct for the individual branching fractions of the f_0 resonances decaying into $\pi^+\pi^-$. *BABAR* measures the relative branching ratios of $f_0(980) \to K^+K^-/\pi^+\pi^-$ of 0.69 ± 0.32 using $B^\pm \to K^\pm K^\pm K^\mp$ and $B^\pm \to K^\pm\pi^\pm\pi^\mp$ decays [36]. The BES Collaboration has extracted relative branching ratios using $\psi(2S) \to \gamma\chi_{c0}$ decays where the $\chi_{c0} \to f_0(980)f_0(980)$, and either both $f_0(980)$'s decay into $\pi^+\pi^-$ or one into $\pi^+\pi^-$ and the other into K^+K^-. Their results [37] are that the relative branching ratio of $f_0(980) \to K^+K^-/\pi^+\pi^-$ is $0.25^{+0.17}_{-0.11}$[38]. Averaging the two measurements gives

$$\frac{\mathcal{B}(f_0(980) \to K^+K^-)}{\mathcal{B}(f_0(980) \to \pi^+\pi^-)} = 0.35^{+0.15}_{-0.14}. \quad (33)$$

Assuming that the $\pi\pi$ and KK decays are dominant we can also extract

$$\mathcal{B}(f_0(980) \to \pi^+\pi^-) = (0.46 \pm 0.06), \quad (34)$$

where we have assumed that the only other decays are to $\pi^0\pi^0$ (one half of the $\pi^+\pi^-$ rate), and to neutral kaons (equal to charged kaons). We use $\mathcal{B}(f_0(500) \to \pi^+\pi^-) = \frac{2}{3}$, which follows from isospin Clebsch-Gordan coefficients, assuming that the only decays are into two pions. Since we have only an upper limit on the $J/\psi f_0(980)$ final state, we will only find an upper limit on the mixing angle, so if any other decay modes of the $f_0(500)$ exist, they would make the limit more stringent.

In order to set an upper limit on $|\varphi_m|$, we simulate the final φ_m measurement using as input the central value of the measured ratio, the full statistical error matrix obtained from the 7R model fit and asymmetric Gaussian random variables different for the positive, $+3.3\%$, and negative, -2.6%, systematic uncertainties (see Table XI). The resulting rate ratios of $f_0(980)$ to $f_0(500)$ are then multiplied by a factor of $\mathcal{B}(f_0(500) \to \pi^+\pi^-)/\mathcal{B}(f_0(980) \to \pi^+\pi^-) \times \frac{\Phi(500)}{\Phi(980)}$ where a Gaussian random variable is used for $\mathcal{B}(f_0(980) \to \pi^+\pi^-)$ to take into account the uncertainty in the measurement shown in Eq. (34). The upper limit at 90% confidence level (C.L.) is determined when 10% of the simulations exceed the limit value. We find

$$\tan^2\varphi_m \equiv r_\sigma^f = (1.1^{+1.2+6.0}_{-0.7-0.7}) \times 10^{-2} < 0.098 \text{ at } 90\% \text{ C.L.},$$

which translates into a limit of

$$|\varphi_m| < 17^\circ \quad \text{at } 90\% \text{ C.L.},$$

where we neglect the effect caused by the small systematic uncertainty on the ratio of phase space factors.

If the scalar meson substructure is tetraquark, the wave functions are

$$|f_0(980)\rangle = \frac{1}{\sqrt{2}}(|[su][\bar{s}\,\bar{u}]\rangle + |[sd][\bar{s}\,\bar{d}]\rangle) \quad (35)$$

$$|f_0(500)\rangle = |[ud][\bar{u}\,\bar{d}]\rangle. \quad (36)$$

The ratio r_σ^f was predicted to be $1/2$ for pure tetraquark states in Ref. [2]. The measured upper limit on r_σ^f of 0.098 at 90% C.L. deviates from the tetraquark prediction by eight standard deviations.

VIII. CONCLUSIONS

We have studied the resonance structure of $\bar{B}^0 \to J/\psi\pi^+\pi^-$ decays using a modified amplitude analysis. The decay distributions are formed by a series of final states described by individual $\pi^+\pi^-$ interfering decay amplitudes. The data are best described by adding coherently the $\rho(770)$, $f_2(1270)$, $f_0(500)$, $\omega(782)$, $\rho(1450)$ and $\rho(1700)$ resonances, with the largest component being the $\rho(770)$. The final state is 56.0% CP even, where we have taken into account both the fit fractions and the interference terms of the different components. Our understanding of the final state composition allows future measurements of CP violation in these resonant final states. These results supersede those obtained in Ref. [4].

There is no evidence for $f_0(980)$ resonance production. We limit the absolute value of the mixing angle between the lightest two scalar states, the $f_0(500)$ and the $f_0(980)$, in the $q\bar{q}$ model to be less than an absolute value of 17° at 90% confidence level. We find that $f_0(980)$ production is much smaller than predicted for tetraquarks, which we rule out at the eight standard deviation level using the model of Ref. [2]. Concern has been expressed [34] that if the $f_0(980)$ were a tetraquark state the measurement of the mixing-dependent CP violating phase in the decay $\bar{B}_s^0 \to J/\psi f_0(980)$ could be affected due to additional decay mechanisms. Our result here alleviates this potential source of error.

ACKNOWLEDGMENTS

We express our gratitude to our colleagues in the CERN accelerator departments for the excellent performance of the LHC. We thank the technical and administrative staff at the LHCb institutes. We acknowledge support from CERN

and from the national agencies: CAPES, CNPq, FAPERJ and FINEP (Brazil); NSFC (China); CNRS/IN2P3 and Region Auvergne (France); BMBF, DFG, HGF and MPG (Germany); SFI (Ireland); INFN (Italy); FOM and NWO (Netherlands); SCSR (Poland); MEN/IFA (Romania); MinES, Rosatom, RFBR and NRC "Kurchatov Institute" (Russia); MinECo, XuntaGal and GENCAT (Spain); SNSF and SER (Switzerland); NASU (Ukraine); STFC and the Royal Society (United Kingdom); and NSF (USA). We also acknowledge the support received from EPLANET, Marie Curie Actions and the ERC under FP7. The Tier1 computing centers are supported by IN2P3 (France), KIT and BMBF (Germany), INFN (Italy), NWO and SURF (Netherlands), PIC (Spain) and GridPP (United Kingdom). We are indebted to the communities behind the multiple open source software packages on which we depend. We are also thankful for the computing resources and the access to software R&D tools provided by Yandex LLC (Russia).

[1] R. Fleischer, Nucl. Instrum. Methods Phys. Res., Sect. A **446**, 1 (2000); S. Faller, M. Jung, R. Fleischer, and T. Mannel, Phys. Rev. D **79**, 014030 (2009).
[2] S. Stone and L. Zhang, Phys. Rev. Lett. **111**, 062001 (2013)
[3] B. Aubert *et al.* (*BABAR* Collaboration), Phys. Rev. Lett. **90**, 091801 (2003); Phys. Rev. D **76**, 031101 (2007)
[4] R. Aaij *et al.* (LHCb Collaboration), Phys. Rev. D **87**, 052001 (2013)
[5] L. Zhang and S. Stone, Phys. Lett. B **719**, 383 (2013).
[6] A. A. Alves, Jr. *et al.* (LHCb Collaboration), JINST **3**, S08005 (2008).
[7] R. Arink *et al.*, JINST **9**, P01002 (2014).
[8] M. Adinolfi *et al.*, Eur. Phys. J. C **73**, 2431 (2013).
[9] A. A. Alves, Jr. *et al.*, JINST **8**, P02022 (2013).
[10] R. Aaij *et al.*, JINST **8**, P04022 (2013).
[11] T. Sjöstrand, S. Mrenna, and P. Skands, J. High Energy Phys. 05 (2006) 026; Comput. Phys. Commun. **178**, 852 (2008).
[12] I. Belyaev *et al.*, *Nuclear Science Symposium Conference Record (NSS/MIC), Knoxville, TN, 2010* (IEEE, Bellingham, WA, 2010), p. 1155.
[13] D. J. Lange, Nucl. Instrum. Methods Phys. Res., Sect. A **462**, 152 (2001).
[14] P. Golonka and Z. Was, Eur. Phys. J. C **45**, 97 (2006).
[15] J. Allison *et al.* (Geant4 Collaboration), IEEE Trans. Nucl. Sci. **53**, 270 (2006).
[16] S. Agostinelli *et al.* (Geant4 Collaboration), Nucl. Instrum. Methods Phys. Res., Sect. A **506**, 250 (2003).
[17] M. Clemencic, G. Corti, S. Easo, C. R Jones, S. Miglioranzi, M. Pappagallo, and P Robbe, J. Phys. Conf. Ser. **331**, 032023 (2011).
[18] U. Nierste, Heavy Quark Physics, in *Lectures at the Helmholtz International Summer School, Dubna, Russia, 2008*; I. I. Bigi and A. Sanda, Cambridge Monogr. Part. Phys., Nucl. Phys., Cosmol. **9**, 1 (2000).
[19] J. Beringer *et al.* (Particle Data Group), Phys. Rev. D **86**, 010001 (2012).
[20] R. Aaij *et al.* (LHCb Collaboration), Phys. Rev. D **86**, 052006 (2012).
[21] R. Mizuk *et al.* (Belle Collaboration), Phys. Rev. D **78**, 072004 (2008).
[22] L. Breiman, J. H. Friedman, R. A. Olshen, and C. J. Stone, *Classification and Regression Trees* (Wadsworth International Group, Belmont, 1984).
[23] T. Skwarnicki, Ph.D. thesis, Institute of Nuclear Physics, [Institution Report No. DESY-F31-86-02, 1986 (unpublished)].
[24] S. Stone and L. Zhang, arXiv:0909.5442
[25] W. D. Hulsbergen, Nucl. Instrum. Methods Phys. Res., Sect. A **552**, 566 (2005).
[26] R. Aaij *et al.* (LHCb Collaboration), Phys. Lett. B **734**, 122 (2014).
[27] S. M. Flatté, Phys. Lett. **63B**, 228 (1976).
[28] R. Aaij *et al.* (LHCb Collaboration), Phys. Rev. D **89**, 092006 (2014).
[29] H. Muramatsu *et al.* (CLEO Collaboration), Phys. Rev. Lett. **89**, 251802 (2002).
[30] S. Baker and R. D. Cousins, Nucl. Instrum. Methods Phys. Res. **221**, 437 (1984).
[31] P. del Amo Sanchez *et al.* (*BABAR* Collaboration), Phys. Rev. D **83**, 052001 (2011).
[32] D. V. Bugg, J. Phys. G **34**, 151 (2007).
[33] G. J. Gounaris and J. J. Sakurai, Phys. Rev. Lett. **21**, 244 (1968).
[34] R. Fleischer, R. Knegjens, and G. Ricciardi, Eur. Phys. J. C **71**, 1832 (2011)
[35] W. Ochs, J. Phys. G **40**, 043001 (2013).
[36] B. Aubert *et al.* (*BABAR* Collaboration), Phys. Rev. D **74**, 032003 (2006).
[37] M. Ablikim *et al.* (BES Collaboration), Phys. Rev. D **70**, 092002 (2004); **72**, 092002 (2005).
[38] K. M. Ecklund *et al.* (CLEO Collaboration), Phys. Rev. D **80**, 052009 (2009).

R. Aaij,[41] B. Adeva,[37] M. Adinolfi,[46] A. Affolder,[52] Z. Ajaltouni,[5] J. Albrecht,[9] F. Alessio,[38] M. Alexander,[51] S. Ali,[41] G. Alkhazov,[30] P. Alvarez Cartelle,[37] A. A. Alves Jr.,[25,38] S. Amato,[2] S. Amerio,[22] Y. Amhis,[7] L. An,[3] L. Anderlini,[17,a] J. Anderson,[40] R. Andreassen,[57] M. Andreotti,[16,b] J. E. Andrews,[58] R. B. Appleby,[54] O. Aquines Gutierrez,[10] F. Archilli,[38]

A. Artamonov,[35] M. Artuso,[59] E. Aslanides,[6] G. Auriemma,[25,c] M. Baalouch,[5] S. Bachmann,[11] J. J. Back,[48] A. Badalov,[36] V. Balagura,[31] W. Baldini,[16] R. J. Barlow,[54] C. Barschel,[38] S. Barsuk,[7] W. Barter,[47] V. Batozskaya,[28] T. Bauer,[41] A. Bay,[39] L. Beaucourt,[4] J. Beddow,[51] F. Bedeschi,[23] I. Bediaga,[1] S. Belogurov,[31] K. Belous,[35] I. Belyaev,[31] E. Ben-Haim,[8] G. Bencivenni,[18] S. Benson,[50] J. Benton,[46] A. Berezhnoy,[32] R. Bernet,[40] M.-O. Bettler,[47] M. van Beuzekom,[41] A. Bien,[11] S. Bifani,[45] T. Bird,[54] A. Bizzeti,[17,d] P. M. Bjørnstad,[54] T. Blake,[48] F. Blanc,[39] J. Blouw,[10] S. Blusk,[59] V. Bocci,[25] A. Bondar,[34] N. Bondar,[30,38] W. Bonivento,[15,38] S. Borghi,[54] A. Borgia,[59] M. Borsato,[7] T. J. V. Bowcock,[52] E. Bowen,[40] C. Bozzi,[16] T. Brambach,[9] J. van den Brand,[42] J. Bressieux,[39] D. Brett,[54] M. Britsch,[10] T. Britton,[59] N. H. Brook,[46] H. Brown,[52] A. Bursche,[40] G. Busetto,[22,e] J. Buytaert,[38] S. Cadeddu,[15] R. Calabrese,[16,b] M. Calvi,[20,f] M. Calvo Gomez,[36,g] A. Camboni,[36] P. Campana,[18,38] D. Campora Perez,[38] A. Carbone,[14,h] G. Carboni,[24,i] R. Cardinale,[19,38,j] A. Cardini,[15] H. Carranza-Mejia,[50] L. Carson,[50] K. Carvalho Akiba,[2] G. Casse,[52] L. Cassina,[20] L. Castillo Garcia,[38] M. Cattaneo,[38] C. Cauet,[9] R. Cenci,[58] M. Charles,[8] P. Charpentier,[38] S.-F. Cheung,[55] N. Chiapolini,[40] M. Chrzaszcz,[40,26] K. Ciba,[38] X. Cid Vidal,[38] G. Ciezarek,[53] P. E. L. Clarke,[50] M. Clemencic,[38] H. V. Cliff,[47] J. Closier,[38] V. Coco,[38] J. Cogan,[6] E. Cogneras,[5] P. Collins,[38] A. Comerma-Montells,[11] A. Contu,[15,38] A. Cook,[46] M. Coombes,[46] S. Coquereau,[8] G. Corti,[38] M. Corvo,[16,b] I. Counts,[56] B. Couturier,[38] G. A. Cowan,[50] D. C. Craik,[48] M. Cruz Torres,[60] S. Cunliffe,[53] R. Currie,[50] C. D'Ambrosio,[38] J. Dalseno,[46] P. David,[8] P. N. Y. David,[41] A. Davis,[57] K. De Bruyn,[41] S. De Capua,[54] M. De Cian,[11] J. M. De Miranda,[1] L. De Paula,[2] W. De Silva,[57] P. De Simone,[18] D. Decamp,[4] M. Deckenhoff,[9] L. Del Buono,[8] N. Déléage,[4] D. Derkach,[55] O. Deschamps,[5] F. Dettori,[42] A. Di Canto,[38] H. Dijkstra,[38] S. Donleavy,[52] F. Dordei,[11] M. Dorigo,[39] A. Dosil Suárez,[37] D. Dossett,[48] A. Dovbnya,[43] F. Dupertuis,[39] P. Durante,[38] R. Dzhelyadin,[35] A. Dziurda,[26] A. Dzyuba,[30] S. Easo,[49,38] U. Egede,[53] V. Egorychev,[31] S. Eidelman,[34] S. Eisenhardt,[50] U. Eitschberger,[9] R. Ekelhof,[9] L. Eklund,[51,38] I. El Rifai,[5] C. Elsasser,[40] S. Ely,[59] S. Esen,[11] T. Evans,[55] A. Falabella,[16,b] C. Färber,[11] C. Farinelli,[41] N. Farley,[45] S. Farry,[52] D. Ferguson,[50] V. Fernandez Albor,[37] F. Ferreira Rodrigues,[1] M. Ferro-Luzzi,[38] S. Filippov,[33] M. Fiore,[16,b] M. Fiorini,[16,b] M. Firlej,[27] C. Fitzpatrick,[38] T. Fiutowski,[27] M. Fontana,[10] F. Fontanelli,[19,j] R. Forty,[38] O. Francisco,[2] M. Frank,[38] C. Frei,[38] M. Frosini,[17,38,a] J. Fu,[21,38] E. Furfaro,[24,i] A. Gallas Torreira,[37] D. Galli,[14,h] S. Gallorini,[22] S. Gambetta,[19,j] M. Gandelman,[2] P. Gandini,[59] Y. Gao,[3] J. Garofoli,[59] J. Garra Tico,[47] L. Garrido,[36] C. Gaspar,[38] R. Gauld,[55] L. Gavardi,[9] E. Gersabeck,[11] M. Gersabeck,[54] T. Gershon,[48] P. Ghez,[4] A. Gianelle,[22] S. Giani',[39] V. Gibson,[47] L. Giubega,[29] V. V. Gligorov,[38] C. Göbel,[60] D. Golubkov,[31] A. Golutvin,[53,31,38] A. Gomes,[1,k] H. Gordon,[38] C. Gotti,[20] M. Grabalosa Gándara,[5] R. Graciani Diaz,[36] L. A. Granado Cardoso,[38] E. Graugés,[36] G. Graziani,[17] A. Grecu,[29] E. Greening,[55] S. Gregson,[47] P. Griffith,[45] L. Grillo,[11] O. Grünberg,[62] B. Gui,[59] E. Gushchin,[33] Y. Guz,[35,38] T. Gys,[38] C. Hadjivasiliou,[59] G. Haefeli,[39] C. Haen,[38] S. C. Haines,[47] S. Hall,[53] B. Hamilton,[58] T. Hampson,[46] X. Han,[11] S. Hansmann-Menzemer,[11] N. Harnew,[55] S. T. Harnew,[46] J. Harrison,[54] T. Hartmann,[62] J. He,[38] T. Head,[38] V. Heijne,[41] K. Hennessy,[52] P. Henrard,[5] L. Henry,[8] J. A. Hernando Morata,[37] E. van Herwijnen,[38] M. Heß,[62] A. Hicheur,[1] D. Hill,[55] M. Hoballah,[5] C. Hombach,[54] W. Hulsbergen,[41] P. Hunt,[55] N. Hussain,[55] D. Hutchcroft,[52] D. Hynds,[51] M. Idzik,[27] P. Ilten,[56] R. Jacobsson,[38] A. Jaeger,[11] J. Jalocha,[55] E. Jans,[41] P. Jaton,[39] A. Jawahery,[58] M. Jezabek,[26] F. Jing,[3] M. John,[55] D. Johnson,[55] C. R. Jones,[47] C. Joram,[38] B. Jost,[38] N. Jurik,[59] M. Kaballo,[9] S. Kandybei,[43] W. Kanso,[6] M. Karacson,[38] T. M. Karbach,[38] M. Kelsey,[59] I. R. Kenyon,[45] T. Ketel,[42] B. Khanji,[20] C. Khurewathanakul,[39] S. Klaver,[54] O. Kochebina,[7] M. Kolpin,[11] I. Komarov,[39] R. F. Koopman,[42] P. Koppenburg,[41,38] M. Korolev,[32] A. Kozlinskiy,[41] L. Kravchuk,[33] K. Kreplin,[11] M. Kreps,[48] G. Krocker,[11] P. Krokovny,[34] F. Kruse,[9] M. Kucharczyk,[20,26,38,f] V. Kudryavtsev,[34] K. Kurek,[28] T. Kvaratskheliya,[31] V. N. La Thi,[39] D. Lacarrere,[38] G. Lafferty,[54] A. Lai,[15] D. Lambert,[50] R. W. Lambert,[42] E. Lanciotti,[38] G. Lanfranchi,[18] C. Langenbruch,[38] B. Langhans,[38] T. Latham,[48] C. Lazzeroni,[45] R. Le Gac,[6] J. van Leerdam,[41] J.-P. Lees,[4] R. Lefèvre,[5] A. Leflat,[32] J. Lefrançois,[7] S. Leo,[23] O. Leroy,[6] T. Lesiak,[26] B. Leverington,[11] Y. Li,[3] M. Liles,[52] R. Lindner,[38] C. Linn,[38] F. Lionetto,[40] B. Liu,[15] G. Liu,[38] S. Lohn,[38] I. Longstaff,[51] J. H. Lopes,[2] N. Lopez-March,[39] P. Lowdon,[40] H. Lu,[3] D. Lucchesi,[22,e] H. Luo,[50] A. Lupato,[22] E. Luppi,[16,b] O. Lupton,[55] F. Machefert,[7] I. V. Machikhiliyan,[31] F. Maciuc,[29] O. Maev,[30] S. Malde,[55] G. Manca,[15,l] G. Mancinelli,[6] M. Manzali,[16,b] J. Maratas,[5] J. F. Marchand,[4] U. Marconi,[14] C. Marin Benito,[36] P. Marino,[23,m] R. Märki,[39] J. Marks,[11] G. Martellotti,[25] A. Martens,[8] A. Martín Sánchez,[7] M. Martinelli,[41] D. Martinez Santos,[42] F. Martinez Vidal,[64] D. Martins Tostes,[2] A. Massafferri,[1] R. Matev,[38] Z. Mathe,[38] C. Matteuzzi,[20] A. Mazurov,[16,b] M. McCann,[53] J. McCarthy,[45] A. McNab,[54] R. McNulty,[12] B. McSkelly,[52] B. Meadows,[57,55] F. Meier,[9] M. Meissner,[11] M. Merk,[41] D. A. Milanes,[8] M.-N.Minard,[4] N. Moggi,[14] J. Molina Rodriguez,[60] S. Monteil,[5] D. Moran,[54] M. Morandin,[22] P. Morawski,[26] A. Mordà,[6] M. J. Morello,[23,m] J. Moron,[27] R. Mountain,[59] F. Muheim,[50] K. Müller,[40] R. Muresan,[29] M. Mussini,[14] B. Muster,[39] P. Naik,[46] T. Nakada,[39] R. Nandakumar,[49] I. Nasteva,[2] M. Needham,[50] N. Neri,[21] S. Neubert,[38] N. Neufeld,[38] M. Neuner,[11]

A. D. Nguyen,[39] T. D. Nguyen,[39] C. Nguyen-Mau,[39,n] M. Nicol,[7] V. Niess,[5] R. Niet,[9] N. Nikitin,[32] T. Nikodem,[11] A. Novoselov,[35] A. Oblakowska-Mucha,[27] V. Obraztsov,[35] S. Oggero,[41] S. Ogilvy,[51] O. Okhrimenko,[44] R. Oldeman,[15,l] G. Onderwater,[65] M. Orlandea,[29] J. M. Otalora Goicochea,[2] P. Owen,[53] A. Oyanguren,[64] B. K. Pal,[59] A. Palano,[13,o] F. Palombo,[21,p] M. Palutan,[18] J. Panman,[38] A. Papanestis,[49,38] M. Pappagallo,[51] C. Parkes,[54] C. J. Parkinson,[9] G. Passaleva,[17] G. D. Patel,[52] M. Patel,[53] C. Patrignani,[19,j] A. Pazos Alvarez,[37] A. Pearce,[54] A. Pellegrino,[41] M. Pepe Altarelli,[38] S. Perazzini,[14,h] E. Perez Trigo,[37] P. Perret,[5] M. Perrin-Terrin,[6] L. Pescatore,[45] E. Pesen,[66] K. Petridis,[53] A. Petrolini,[19,j] E. Picatoste Olloqui,[36] B. Pietrzyk,[4] T. Pilař,[48] D. Pinci,[25] A. Pistone,[19] S. Playfer,[50] M. Plo Casasus,[37] F. Polci,[8] A. Poluektov,[48,34] E. Polycarpo,[2] A. Popov,[35] D. Popov,[10] B. Popovici,[29] C. Potterat,[2] A. Powell,[55] J. Prisciandaro,[39] A. Pritchard,[52] C. Prouve,[46] V. Pugatch,[44] A. Puig Navarro,[39] G. Punzi,[23,q] W. Qian,[4] B. Rachwal,[26] J. H. Rademacker,[46] B. Rakotomiaramanana,[39] M. Rama,[18] M. S. Rangel,[2] I. Raniuk,[43] N. Rauschmayr,[38] G. Raven,[42] S. Reichert,[54] M. M. Reid,[48] A. C. dos Reis,[1] S. Ricciardi,[49] A. Richards,[53] M. Rihl,[38] K. Rinnert,[52] V. Rives Molina,[36] D. A. Roa Romero,[5] P. Robbe,[7] A. B. Rodrigues,[1] E. Rodrigues,[54] P. Rodriguez Perez,[54] S. Roiser,[38] V. Romanovsky,[35] A. Romero Vidal,[37] M. Rotondo,[22] J. Rouvinet,[39] T. Ruf,[38] F. Ruffini,[23] H. Ruiz,[36] P. Ruiz Valls,[64] G. Sabatino,[25,i] J. J. Saborido Silva,[37] N. Sagidova,[30] P. Sail,[51] B. Saitta,[15,l] V. Salustino Guimaraes,[2] C. Sanchez Mayordomo,[64] B. Sanmartin Sedes,[37] R. Santacesaria,[25] C. Santamarina Rios,[37] E. Santovetti,[24,i] M. Sapunov,[6] A. Sarti,[18,r] C. Satriano,[25,c] A. Satta,[24] M. Savrie,[16,b] D. Savrina,[31,32] M. Schiller,[42] H. Schindler,[38] M. Schlupp,[9] M. Schmelling,[10] B. Schmidt,[38] O. Schneider,[39] A. Schopper,[38] M.-H. Schune,[7] R. Schwemmer,[38] B. Sciascia,[18] A. Sciubba,[25] M. Seco,[37] A. Semennikov,[31] K. Senderowska,[27] I. Sepp,[53] N. Serra,[40] J. Serrano,[6] L. Sestini,[22] P. Seyfert,[11] M. Shapkin,[35] I. Shapoval,[16,43,b] Y. Shcheglov,[30] T. Shears,[52] L. Shekhtman,[34] V. Shevchenko,[63] A. Shires,[9] R. Silva Coutinho,[48] G. Simi,[22] M. Sirendi,[47] N. Skidmore,[46] T. Skwarnicki,[59] N. A. Smith,[52] E. Smith,[55,49] E. Smith,[53] J. Smith,[47] M. Smith,[54] H. Snoek,[41] M. D. Sokoloff,[57] F. J. P. Soler,[51] F. Soomro,[39] D. Souza,[46] B. Souza De Paula,[2] B. Spaan,[9] A. Sparkes,[50] F. Spinella,[23] P. Spradlin,[51] F. Stagni,[38] S. Stahl,[11] O. Steinkamp,[40] O. Stenyakin,[35] S. Stevenson,[55] S. Stoica,[29] S. Stone,[59] B. Storaci,[40] S. Stracka,[23,38] M. Straticiuc,[29] U. Straumann,[40] R. Stroili,[22] V. K. Subbiah,[38] L. Sun,[57] W. Sutcliffe,[53] K. Swientek,[27] S. Swientek,[9] V. Syropoulos,[42] M. Szczekowski,[28] P. Szczypka,[39,38] D. Szilard,[2] T. Szumlak,[27] S. T'Jampens,[4] M. Teklishyn,[7] G. Tellarini,[16,b] F. Teubert,[38] C. Thomas,[55] E. Thomas,[38] J. van Tilburg,[41] V. Tisserand,[4] M. Tobin,[39] S. Tolk,[42] L. Tomassetti,[16,b] D. Tonelli,[38] S. Topp-Joergensen,[55] N. Torr,[55] E. Tournefier,[4] S. Tourneur,[39] M. T. Tran,[39] M. Tresch,[40] A. Tsaregorodtsev,[6] P. Tsopelas,[41] N. Tuning,[41] M. Ubeda Garcia,[38] A. Ukleja,[28] A. Ustyuzhanin,[63] U. Uwer,[11] V. Vagnoni,[14] G. Valenti,[14] A. Vallier,[7] R. Vazquez Gomez,[18] P. Vazquez Regueiro,[37] C. Vázquez Sierra,[37] S. Vecchi,[16] J. J. Velthuis,[46] M. Veltri,[17,s] G. Veneziano,[39] M. Vesterinen,[11] B. Viaud,[7] D. Vieira,[2] M. Vieites Diaz,[37] X. Vilasis-Cardona,[36,g] A. Vollhardt,[40] D. Volyanskyy,[10] D. Voong,[46] A. Vorobyev,[30] V. Vorobyev,[34] C. Voß,[62] H. Voss,[10] J. A. de Vries,[41] R. Waldi,[62] C. Wallace,[48] R. Wallace,[12] J. Walsh,[23] S. Wandernoth,[11] J. Wang,[59] D. R. Ward,[47] N. K. Watson,[45] D. Websdale,[53] M. Whitehead,[48] J. Wicht,[38] D. Wiedner,[11] G. Wilkinson,[55] M. P. Williams,[45] M. Williams,[56] F. F. Wilson,[49] J. Wimberley,[58] J. Wishahi,[9] W. Wislicki,[28] M. Witek,[26] G. Wormser,[7] S. A. Wotton,[47] S. Wright,[47] S. Wu,[3] K. Wyllie,[38] Y. Xie,[61] Z. Xing,[59] Z. Xu,[39] Z. Yang,[3] X. Yuan,[3] O. Yushchenko,[35] M. Zangoli,[14] M. Zavertyaev,[10,t] F. Zhang,[3] L. Zhang,[59] W. C. Zhang,[12] Y. Zhang,[3] A. Zhelezov,[11] A. Zhokhov,[31] L. Zhong[3] and A. Zvyagin[38]

(LHCb Collaboration)

[1]*Centro Brasileiro de Pesquisas Físicas (CBPF), Rio de Janeiro, Brazil*
[2]*Universidade Federal do Rio de Janeiro (UFRJ), Rio de Janeiro, Brazil*
[3]*Center for High Energy Physics, Tsinghua University, Beijing, China*
[4]*LAPP, Université de Savoie, CNRS/IN2P3, Annecy-Le-Vieux, France*
[5]*Clermont Université, Université Blaise Pascal, CNRS/IN2P3, LPC, Clermont-Ferrand, France*
[6]*CPPM, Aix-Marseille Université, CNRS/IN2P3, Marseille, France*
[7]*LAL, Université Paris-Sud, CNRS/IN2P3, Orsay, France*
[8]*LPNHE, Université Pierre et Marie Curie, Université Paris Diderot, CNRS/IN2P3, Paris, France*
[9]*Fakultät Physik, Technische Universität Dortmund, Dortmund, Germany*
[10]*Max-Planck-Institut für Kernphysik (MPIK), Heidelberg, Germany*
[11]*Physikalisches Institut, Ruprecht-Karls-Universität Heidelberg, Heidelberg, Germany*
[12]*School of Physics, University College Dublin, Dublin, Ireland*
[13]*Sezione INFN di Bari, Bari, Italy*

[14]*Sezione INFN di Bologna, Bologna, Italy*
[15]*Sezione INFN di Cagliari, Cagliari, Italy*
[16]*Sezione INFN di Ferrara, Ferrara, Italy*
[17]*Sezione INFN di Firenze, Firenze, Italy*
[18]*Laboratori Nazionali dell'INFN di Frascati, Frascati, Italy*
[19]*Sezione INFN di Genova, Genova, Italy*
[20]*Sezione INFN di Milano Bicocca, Milano, Italy*
[21]*Sezione INFN di Milano, Milano, Italy*
[22]*Sezione INFN di Padova, Padova, Italy*
[23]*Sezione INFN di Pisa, Pisa, Italy*
[24]*Sezione INFN di Roma Tor Vergata, Roma, Italy*
[25]*Sezione INFN di Roma La Sapienza, Roma, Italy*
[26]*Henryk Niewodniczanski Institute of Nuclear Physics Polish Academy of Sciences, Kraków, Poland*
[27]*AGH University of Science and Technology, Faculty of Physics and Applied Computer Science, Kraków, Poland*
[28]*National Center for Nuclear Research (NCBJ), Warsaw, Poland*
[29]*Horia Hulubei National Institute of Physics and Nuclear Engineering, Bucharest-Magurele, Romania*
[30]*Petersburg Nuclear Physics Institute (PNPI), Gatchina, Russia*
[31]*Institute of Theoretical and Experimental Physics (ITEP), Moscow, Russia*
[32]*Institute of Nuclear Physics, Moscow State University (SINP MSU), Moscow, Russia*
[33]*Institute for Nuclear Research of the Russian Academy of Sciences (INR RAN), Moscow, Russia*
[34]*Budker Institute of Nuclear Physics (SB RAS) and Novosibirsk State University, Novosibirsk, Russia*
[35]*Institute for High Energy Physics (IHEP), Protvino, Russia*
[36]*Universitat de Barcelona, Barcelona, Spain*
[37]*Universidad de Santiago de Compostela, Santiago de Compostela, Spain*
[38]*European Organization for Nuclear Research (CERN), Geneva, Switzerland*
[39]*Ecole Polytechnique Fédérale de Lausanne (EPFL), Lausanne, Switzerland*
[40]*Physik-Institut, Universität Zürich, Zürich, Switzerland*
[41]*Nikhef National Institute for Subatomic Physics, Amsterdam, The Netherlands*
[42]*Nikhef National Institute for Subatomic Physics and VU University Amsterdam, Amsterdam, The Netherlands*
[43]*NSC Kharkiv Institute of Physics and Technology (NSC KIPT), Kharkiv, Ukraine*
[44]*Institute for Nuclear Research of the National Academy of Sciences (KINR), Kyiv, Ukraine*
[45]*University of Birmingham, Birmingham, United Kingdom*
[46]*H. H. Wills Physics Laboratory, University of Bristol, Bristol, United Kingdom*
[47]*Cavendish Laboratory, University of Cambridge, Cambridge, United Kingdom*
[48]*Department of Physics, University of Warwick, Coventry, United Kingdom*
[49]*STFC Rutherford Appleton Laboratory, Didcot, United Kingdom*
[50]*School of Physics and Astronomy, University of Edinburgh, Edinburgh, United Kingdom*
[51]*School of Physics and Astronomy, University of Glasgow, Glasgow, United Kingdom*
[52]*Oliver Lodge Laboratory, University of Liverpool, Liverpool, United Kingdom*
[53]*Imperial College London, London, United Kingdom*
[54]*School of Physics and Astronomy, University of Manchester, Manchester, United Kingdom*
[55]*Department of Physics, University of Oxford, Oxford, United Kingdom*
[56]*Massachusetts Institute of Technology, Cambridge, Massachusetts 02139-4307, USA*
[57]*University of Cincinnati, Cincinnati, Ohio 45221-0011, USA*
[58]*University of Maryland, College Park, Maryland 20742, USA*
[59]*Syracuse University, Syracuse, New York 13244-1130, USA*
[60]*Pontifícia Universidade Católica do Rio de Janeiro (PUC-Rio), Rio de Janeiro, Brazil (associated with Institution Universidade Federal do Rio de Janeiro (UFRJ), Rio de Janeiro, Brazil)*
[61]*Institute of Particle Physics, Central China Normal University, Wuhan, Hubei, China (associated with Institution Center for High Energy Physics, Tsinghua University, Beijing, China)*
[62]*Institut für Physik, Universität Rostock, Rostock, Germany (associated with Institution Physikalisches Institut, Ruprecht-Karls-Universität Heidelberg, Heidelberg, Germany)*
[63]*National Research Centre Kurchatov Institute, Moscow, Russia (associated with Institution Institute of Theoretical and Experimental Physics (ITEP), Moscow, Russia)*

[64]*Instituto de Fisica Corpuscular (IFIC), Universitat de Valencia-CSIC, Valencia, Spain*
(associated with Institution Universitat de Barcelona, Barcelona, Spain)
[65]*KVI-University of Groningen, Groningen, The Netherlands*
(associated with Institution Nikhef National Institute for Subatomic Physics, Amsterdam, The Netherlands)
[66]*CBU-Manisa, Manisa, Turkey*
(associated with Institution European Organization for Nuclear Research (CERN), Geneva, Switzerland)

[a]Also at Università di Firenze, Firenze, Italy.
[b]Also at Università di Ferrara, Ferrara, Italy.
[c]Also at Università della Basilicata, Potenza, Italy.
[d]Also at Università di Modena e Reggio Emilia, Modena, Italy.
[e]Also at Università di Padova, Padova, Italy.
[f]Also at Università di Milano Bicocca, Milano, Italy.
[g]Also at LIFAELS, La Salle, Universitat Ramon Llull, Barcelona, Spain.
[h]Also at Università di Bologna, Bologna, Italy.
[i]Also at Università di Roma Tor Vergata, Roma, Italy.
[j]Also at Università di Genova, Genova, Italy.
[k]Also at Universidade Federal do Triângulo Mineiro (UFTM), Uberaba-MG, Brazil.
[l]Also at Università di Cagliari, Cagliari, Italy.
[m]Also at Scuola Normale Superiore, Pisa, Italy.
[n]Also at Hanoi University of Science, Hanoi, Viet Nam.
[o]Also at Università di Bari, Bari, Italy.
[p]Also at Università degli Studi di Milano, Milano, Italy.
[q]Also at Università di Pisa, Pisa, Italy.
[r]Also at Università di Roma La Sapienza, Roma, Italy.
[s]Also at Università di Urbino, Urbino, Italy.
[t]Also at P. N. Lebedev Physical Institute, Russian Academy of Science (LPI RAS), Moscow, Russia.